REPORT DOCUMENTATION PAGE

AFRL-SR-AR-TR-09-0201

1. REPORT DATE *(DD-MM-YYYY)*	2. REPORT TYPE	3. DATES COVERED *(From - To)*
15-02-2009	FINAL REPORT	1-03-06 - 30-11-08

4. TITLE AND SUBTITLE
Toward Adaptive Optic Mitigation of Aero-Optic Effects

5a. CONTRACT NUMBER

5b. GRANT NUMBER
F49550-06-1-0160

5c. PROGRAM ELEMENT NUMBER

6. AUTHOR(S)
ERIC J. JUMPER

5d. PROJECT NUMBER

5e. TASK NUMBER

5f. WORK UNIT NUMBER

7. PERFORMING ORGANIZATION NAME(S) AND ADDRESS(ES)

DEPARTMENT OF AEROSPACE AND
MECHANICAL ENGINEERING
UNIVERSITY OF NOTRE DAME
NOTRE DAME, IN 46556

8. PERFORMING ORGANIZATION REPORT NUMBER

9. SPONSORING / MONITORING AGENCY NAME(S) AND ADDRESS(ES)
AIR FORCE OFFICE OF SIENTIFIC
RESEARCH, AFOSR/NA
875 North Randolph St.
Suite 325, Room 3112
ARLINGTON, VA 22203-1768

10. SPONSOR/MONITOR'S ACRONYM(S)

11. SPONSOR/MONITOR'S REPORT NUMBER(S)

12. DISTRIBUTION / AVAILABILITY STATEMENT

DISTRIBUTION A: APPROVED FOR PUBLIC RELEASE

13. SUPPLEMENTARY NOTES

14. ABSTRACT This report describes aero-optic research at the University of Notre Dame. When a laser beam propagates through a variable-index-of-refraction, turbulent fluid, its wavefront becomes aberrated, reducing associated optical-system performance. For flight Mach numbers as low as 0.3 Mach, turbulence in the flow past the aircraft become important in aberrating wavefronts (aero-optics). This report briefly reviews the mechanisms responsible for these aberrations in free-shear-layer flows. The report begins with describing an historic demonstration performed under this effort that combined the use of flow control and feed-forward adaptive optics to correct the aberrations imposed on an otherwise collimated laser beam projected through a heated jet and a Mach 0.8 free shear layer, respectively; this historic demonstration included a man in the loop. The report then describes the development of an automated control system that removes the man in the loop. Also described is some additional work performed under this grant that examined a spatial-filter approach to analyzing the effect of apertures on several aspects of laser-beam control.

15. SUBJECT TERMS
Aero-Optics, Fluid-Optic Interactions, Adaptive Optics, Wavefront Sensing, Compressible Shear Layers, Flow Control, Mixing Layers, Turbulence, Weakly-Compressible Model,

16. SECURITY CLASSIFICATION OF: UNCLASSIFIED			17. LIMITATION OF ABSTRACT	18. NUMBER OF PAGES	19a. NAME OF RESPONSIBLE PERSON
					John D. Schmisseur, Ph.D.
a. REPORT UNCLASSIFIED	b. ABSTRACT UNCLASSIFIED	c. THIS PAGE UNCLASSIFIED	UL	60 including title page	19b. TELEPHONE NUMBER *(include area code)* (703) 696-6962

TOWARD ADAPTIVE OPTIC MITIGATION OF AERO-OPTIC EFFECTS

Final Report

AFOSR Grant F49550-06-1-0160

Period Covered:
1 March 2006 – 30 November 2008

Principal Investigator: Eric J. Jumper

Center for Flow Physics and Control
Hessert Laboratory
Department of Aerospace and Mechanical Engineering
University of Notre Dame
Notre Dame, Indiana 46556
USA

(574) 631-7680
FAX: (574) 631-8355

Email: jumper.1@nd.edu

27 February 2009

REPORT DOCUMENTATION PAGE

Form Approved
OMB No. 0704-0188

1. REPORT DATE *(DD-MM-YYYY)*	2. REPORT TYPE	3. DATES COVERED *(From - To)*
15-02-2009	FINAL REPORT	1-03-06 - 30-11-08

4. TITLE AND SUBTITLE
Toward Adaptive Optic Mitigation of Aero-Optic Effects

5a. CONTRACT NUMBER

5b. GRANT NUMBER
F49550-06-1-0160

5c. PROGRAM ELEMENT NUMBER

6. AUTHOR(S)
ERIC J. JUMPER

5d. PROJECT NUMBER

5e. TASK NUMBER

5f. WORK UNIT NUMBER

7. PERFORMING ORGANIZATION NAME(S) AND ADDRESS(ES)

DEPARTMENT OF AEROSPACE AND
MECHANICAL ENGINEERING
UNIVERSITY OF NOTRE DAME
NOTRE DAME, IN 46556

8. PERFORMING ORGANIZATION REPORT NUMBER

9. SPONSORING / MONITORING AGENCY NAME(S) AND ADDRESS(ES)
AIR FORCE OFFICE OF SIENTIFIC
RESEARCH, AFOSR/NA
875 North Randolph St.
Suite 325, Room 3112
ARLINGTON, VA 22203-1768

10. SPONSOR/MONITOR'S ACRONYM(S)

11. SPONSOR/MONITOR'S REPORT NUMBER(S)

12. DISTRIBUTION / AVAILABILITY STATEMENT
UL

13. SUPPLEMENTARY NOTES

14. ABSTRACT This report describes aero-optic research at the University of Notre Dame. When a laser beam propagates through a variable-index-of-refraction, turbulent fluid, its wavefront becomes aberrated, reducing associated optical-system performance. For flight Mach numbers as low as 0.3 Mach, turbulence in the flow past the aircraft become important in aberrating wavefronts (aero-optics). This report briefly reviews the mechanisms responsible for these aberrations in free-shear-layer flows. The report begins with describing an historic demonstration performed under this effort that combined the use of flow control and feed-forward adaptive optics to correct the aberrations imposed on an otherwise collimated laser beam projected through a heated jet and a Mach 0.8 free shear layer, respectively; this historic demonstration included a man in the loop. The report then describes the development of an automated control system that removes the man in the loop. Also described is some additional work performed under this grant that examined a spatial-filter approach to analyzing the effect of apertures on several aspects of laser-beam control.

15. SUBJECT TERMS
Aero-Optics, Fluid-Optic Interactions, Adaptive Optics, Wavefront Sensing, Compressible Shear Layers, Flow Control, Mixing Layers, Turbulence, Weakly-Compressible Model, Adaptive Optics

16. SECURITY CLASSIFICATION OF: UNCLASSIFIED			17. LIMITATION OF ABSTRACT	18. NUMBER OF PAGES	19a. NAME OF RESPONSIBLE PERSON
					John D. Schmisseur, Ph.D.
a. REPORT UNCLASSIFIED	b. ABSTRACT UNCLASSIFIED	c. THIS PAGE UNCLASSIFIED	UL	60 including title page	19b. TELEPHONE NUMBER *(include area code)* (703) 696-6962

ABSTRACT

When a laser beam with an otherwise planar optical wavefront, is made to propagate through a turbulent, variable-index flow field, the beam's wavefront is imprinted with a time-varying aberrations over its aperture (beam diameter). These dynamic aberrations degrade the ability for the beam to be focused in the far field. In the case of a laser propagated from an airborne platform, the far field could be anywhere from kilometers to hundreds of kilometers away. The effectiveness of an airborne laser system depends on the beam-control system being able to hold a spot on the far-field aim point, which exceeds a minimum intensity. The beam's intensity in the far field is directly dependent on how well it can be focused. In general, there are two distinct regimes of variant-index flows that contribute to the focus-ability: the first is the beam's path from just outside the flowfield surrounding the aircraft, through the intervening atmosphere, to the far field; and the second is the flow traversed by the beam within the immediate vicinity of the aircraft. The first regime is referred to as "atmospheric propagation." This grant effort specifically addressed the second regime, the optical-propagation problem in the immediate vicinity of an airborne platform; this regime of the optical-propagation problem is referred to as "aero-optics." AFOSR-funded research at Notre Dame has shown that, although propagation through attached turbulent boundary layers can reduce the average on-axis intensity in the far field by 5 – 30%, this reduction in intensity pales in comparison to propagation through a separated shear layer, which can reduce the intensity in the far field by more than 95%. Adaptive optic systems have been used for decades to correct for the aberrations on a beam due to propagation through the atmosphere. These systems, in their conventional architecture, first sense the wavefront aberration that will be imposed on the laser beam propagating through the aberrating field, construct a conjugate waveform to correct for the aberrations, and finally deform a mirror onto which the laser is reflected prior to projection through the aberrating flow. Because the frequencies associated with aero-optical flows are orders of magnitude greater than state-of-the-art, conventional adaptive optic systems, it had been believed that adaptive-optic correction for aero-optic effects could not be done.

The results of the research reported here begin with a successful demonstration of a feed-forward approach to correcting the beam. The approach incorporated flow control to regularize a Mach 0.78 compressible shear layer and used a man-in-the-loop approach to phase up and adjust the amplitude of a traveling waveform being fed forward to Notre Dame's deformable mirror. The experiments demonstrated that the intensity on target in the far field could be increased from 14% of the diffraction-limited intensity uncorrected to 70% of the diffraction-limited intensity after correction. An additional result reported here dealt with the development of an automated controller to replace the man in the loop. Finally, a large part of this report describes results from a theoretical analysis of the effect that apertures play as spatial filters on the aero-optically-imposed aberrations. This section is fairly complete, as it provides guidelines for many of the parameters needed to design adaptive optic systems. It also provides a rational basis for many anomalous findings in the general field of beam control. It is our hope that this report, particularly this last section will be widely circulated to the laser community in the DoD.

TABLE OF CONTENTS

I. INTRODUCTION

When a collimated laser beam of wavelength ~ 1 μm propagates through a separated shear layer with a convective Mach number as low as 0.15 (high speed side at M = 0.3) the beam's wavefront is aberrated to the point that its focused intensity can be reduced by more than 50% of its diffraction-limited intensity. The study of the aberrating effect of shear flows is referred to as *Aero-Optics*.[1] Notre Dame has been studying aero-optics since 1993 (F49620-93-0163, F49620-97-1-0489, F49620-00-1-0025 and F49620-03-1-0019) and has made many breakthroughs. The Notre Dame efforts have moved the understanding of aero-optics from a statistically-based, time-averaged, optical-path-difference (OPD) approach, based on statistical, fluid-mechanical measurements, to a formal, cause-and-effect understanding of optical propagation through boundary and shear layers.[1,2,3] The work reported here made use of the results of these previous grants, in particular the knowledge of the aberrating physics, various high-bandwidth wavefront-sensing instruments developed at Notre Dame, techniques developed using other commercially-available instruments, and our high-bandwidth deformable mirror, acquired under a DURIP grant as part of our high-bandwidth adaptive optics system to demonstrate the historic adaptive-optic correction of a laser beam projected through a Mach 0.8 shear layer. This demonstration took place at the very beginning of the present grant.

Objectives. The objectives of this grant were to make use of forcing to "regularize" a high subsonic-Mach-number shear layer, developed in the last grant, and to make use of the characterization of the concomitant optical environment on a large-aperture laser beam propagated through the regularized shear layer to perform the feed-forward adaptive-optic demonstration referred to above. In parallel with this demonstration that involved a man in the loop, the second primary objective was to develop an automated control system to remove the need for a man in the loop. Additionally, as has been our practice in all our AFOSR grants, where interesting lines of inquiry present themselves we attempt to pursue them; in the present grant this took the form of studying the spatial-filter characteristics of the aperture placed on the laser beam prior to propagating it through the shear layer. As this aperture effect is critical to any control system, it fell within the general context of the present grant.

Approach. The approaches to achieving the grant objectives were to perform a man-in-the-loop demonstration of a feed-forward correction of a relatively large-aperture laser beam aberrated by being propagated through a regularized compressible shear layer. Next, the optical characterization of the regularized shear layer and its velocity field were used to validate the use of a low-order CFD model. Having a sufficiently-faithful CFD model, the characteristics of laser beams numerically propagated through the computed shear layer were used to model control-system architectures for feeding forward to a deformable mirror the conjugate waveforms needed to correct the laser beam. Finally, making use of a successful architecture, hardware was developed that can be used to replace the man in the loop in the shear layer experiments using Notre Dame's feed-forward adaptive-optic mitigation approach for regularized aberrating flows.

II. BACKGROUND

Aero-Optics. The projeetion of a eollimated laser beam, of "viewing aperture" A_p, through a turbulent flowfield with index-of-refraetion variations, leads to a time-varying aberration of its otherwise-planar, optieal wavefront. These aberrations lead to a reduction in performance of an optieal system making use of the optical "information" eontained over the viewing aperture. Systems eoneerned with sueh reduetion in performanee inelude, but are not limited to, airborne laser irradiating systems.

A system's performance reduetion (induced by turbulent, variant-index flowfields) ean be quantified by analysis of the far-field irradiance pattern. [5] The irradiance pattern is the instantaneous intensity pattern at the target, $I(x,y,t)$, where $(0,0)$ would indieate the eenter of the aim point. The extent to whieh the on-axis intensity is reduced as a funetion of time, $I(0,0,t)$, when divided by the highest possible on-axis intensity without aberrations (referred to as the diffraction-limited intensity), I_o, is expressed as the Strehl ratio, SR,

$$SR(t) = \frac{I(0,0,t)}{I_o} \qquad (2\text{-}1)$$

The reduetion in Strehl ratio due to time-varying, aberrating flowfields ean oeeur over short path lengths in the *near field* (i.e., path length, z, on the order of A_p), or it ean oeeur over extended paths (i.e., path lengths, z, much larger than A_p). The former, short-path (near-field) aberration is usually termed *aero-optics* and the latter, long-path aberrations are usually termed *atmospheric propagation*. These classifications have their origin in the speeifie applications with whieh they are assoeiated [see Refs. 6 and 7, for example]. It has long been known that plaeing a eonjugate waveform on the beam prior to its transmission through the aberrating medium results in the emergenee of a planar-wavefront beam as it leaves the medium; systems that sense the aberration, eonstruet and apply the proper eonjugate waveform at regular time intervals are termed *adaptive-optic systems*, and the study of sueh systems is known as *adaptive optics*. [8] The determination of the design requirements for sueh systems depends on understanding the spatial and temporal frequencies of the distorted optieal wavefront for the applieable aberrating flowfields.

Over the last two deeades progress has been made in both measuring the wavefront dynamies for the atmospheric propagation problem and using this information for designing and applying adaptive-optie equipment and techniques. [9] For aero-optie problems, on the other hand, until Notre Dame's sueeessful demonstrations reported here, *no adaptive optic correction for the aero-optic problem was ever demonstrated.* The reason for the inability to correet for aero-optie aberrations prior to work reported here is that the required spatial and temporal frequencies associated with aero-optic problems are at least an order of magnitude greater than those correctable by the eonventional approaeh to designing adaptive-optie systems, even for relatively-slow laboratory flows. [10] As such, the main research thrust in aero-optics until the early to mid 1990's had been to attempt to quantify the time-averaged phase variance (or root-mean-square Optical Path Difference, OPD_{rms}, whieh is related to the phase varianee through the wave number). Once obtained by whatever means, the phase variance was used to compute *an estimate* of the system degradation imposed by the near-field aberrations using the large-aperture approximation. [1] These statistieal methods gave no information useful to the design of adaptive-optie systems required to correet aero-optie aberrations. Researeh at Notre Dame

supported by AFOSR has focused exclusively on the *aero-optics problem*, with an emphasis on understanding how *adaptive optics* can be applied to the problem. As will be described later in this report, Notre Dame has introduced flow control into the adaptive-optic paradigm and developed a feed-forward approach that has now demonstrated a historic first, the adaptive-optic correction of a laser propagated through an otherwise devastating Mach 0.8 free shear layer.

Characteristics of Aero-Optic Aberrations. During a previous AFOSR grant, Notre Dame used a wavefront sensor developed in-house to measure the first-ever, time-resolved wavefront dynamics for laser propagation through the Mach 0.8 compressible shear layer at the Arnold Engineering Development Center (AEDC). [11,12] Figure 1 shows two example time series of measured one-dimensional wavefronts from those tests (5 cm aperture); these data were taken at two stations, Station 1, right at the splitter plate, and Station 2, half a meter downstream from the splitter plate. What is most noteworthy in the data shown in Fig. 1 is the difference in aberration extent between the Station 1 and Station 2 data. The Station 1 data is due to the turbulent boundary layer feeding the shear layer and/or over the extraction window. Even without boundary layer treatment to remove these aberrations, the level of aberration is quite low. For a one-micron-wavelength beam the Strehl ratio can be estimated to be ~ 0.91 using the large-aperture approximation. It might be noted that the Station 2 data contains cyclic tilt, but even when this is removed, computed far-field patterns yielded a time-averaged Strehl ratio of < 0.1. [12] Realistic beam diameters for a HEL system will not be smaller than 20 cm, and when the wavefronts are extended to apertures, *Ap*, greater than 20 cm the OPD_{rms} increases to 0.43 μm, further reducing the Strehl ratio.

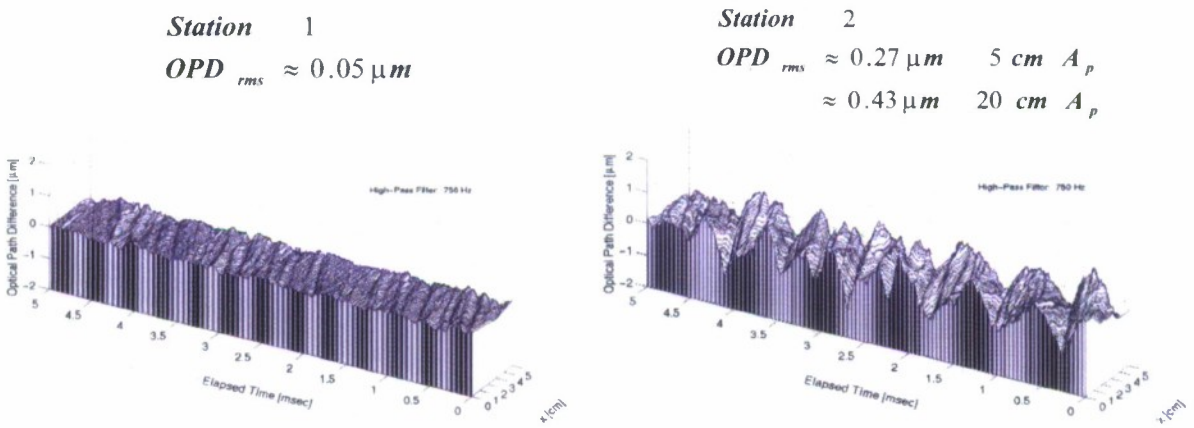

Figure 1. Wavefront Measurements Taken for Propagation through the AEDC Compressible Shear Layer Facility at a Simulated Flight Mach Number of 0.8 at 13,500 ft [Refs. 11,12].

Cause of Aero-Optic Aberrations. Not only were the AEDC data the first of their kind, the wavefronts at 0.5 m from the separation point presented a far-larger aberration environment than was expected due to the then-believed cause of the aberrations in turbulent shear layers. Discovering the cause of the aberrations became the objective of our second AFOSR grant and the result of that investigation led to the now universally-

accepted cause referred to as the *Weakly-Compressible Model*. [2] The key realization at the heart of the Weakly-Compressible Model is the fact that because of the Kelvin Helmholtz instability, free shear layers naturally form coherent structures and, in a frame convecting with the layer, the flow in the coherent structures has high curvature (see Fig. 2). [1,2] This curvature has a concomitant pressure gradient that lowers the pressure at the center of the structures (by several *psi* in the case of near-transonic shear layers). The low pressure is accompanied by a reduction in the density, which in turn lowers the index of refraction. It is this variation in the index of refraction due to the coherent flow structures and the accompanying high pressure/density in the braid connecting adjacent structures that cause most of the aero-optic aberrations in weakly-compressible shear layers. As discussed in Reference 2, all other aberrating influences present in a shear layer, fed by a common total temperature, have effects that add up to only a small fraction of this principal cause. Although, this cause-and-effect explanation appears to be straightforward, it had long been thought (i.e., common knowledge) that static-pressure variations in a free shear layer were negligible (the so-called Strong Reynolds Analogy); the Weakly-Compressible Model argues exactly the opposite.

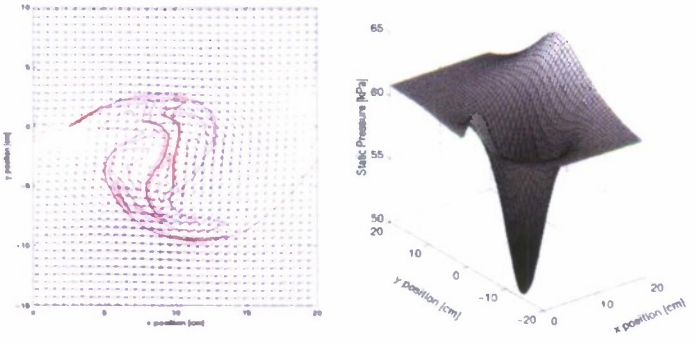

Figure 2. Coherent structure at an Instant in Time, its Flow field as seen in the Convective Frame and its Concomitant Pressure Well as Computed by the Weakly-Compressible Model [Ref. 2].

When the model was used to compute the AEDC conditions, it showed excellent agreement in the large-scale structures, but did not predict the higher-frequency aberrations on the wavefront data. Further analysis convinced us that the higher-frequency aberrations were due to the turbulent boundary layer over the extraction window of the tunnel. To simulate the addition of the boundary layer aberrations, an aberration time series from AEDC Station 1 (as that on the left of Fig. 1, which is due to a turbulent boundary layer) was added to the Weakly-Compressible Model predictions. The comparisons are shown in Fig. 3, which shows the simulation for the AEDC Station 2 conditions in the upper left hand, the AEDC Station 2 data in the lower right hand, and the result of adding the Station 1 wavefronts (upper right hand) to the simulations, resulting in the lower left hand time series. It is clear that the two bottom time series, the simulation and the data, compare well. [2] Having the model enabled us to infer that the tilt in the Station 2 data was really a ramification of a larger coherent structure convecting past the 5 cm aperture used in the AEDC experiments. Using our model, we were also able to show that over the larger aperture the OPD_{rms} increases to ~0.43 μm, none of which can be removed by tilt corrections. In this case the Strehl ratio dropped to 0.011. [13] Finally, with the help of the model, we were able to scale the aberration effects

measured at the AEDC conditions over the small 5 cm aperture, not only to larger apertures, but also to other altitudes and Mach numbers. [14]

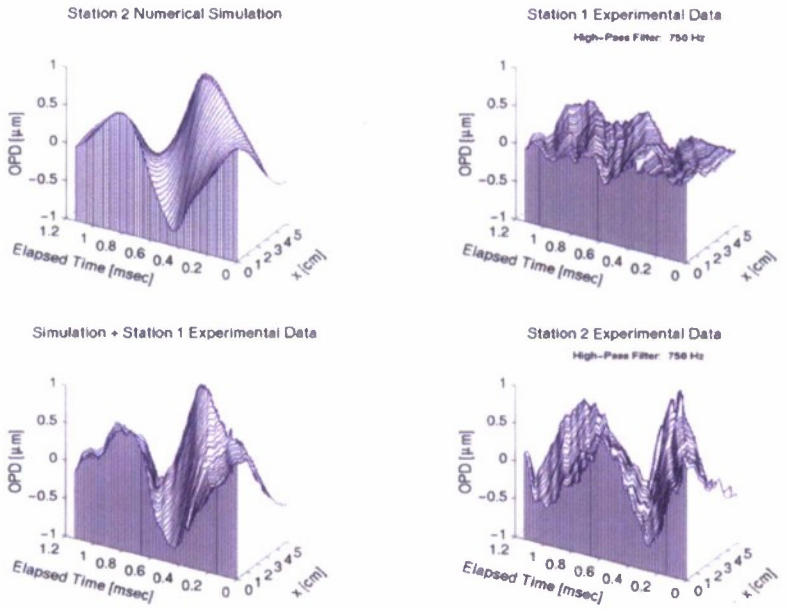

Figure 3. Example Time Series of Wavefronts: the Weakly-Compressible-Model-computed wavefronts for the AEDC, Station 2 conditions (upper left); compared to the Station 2 experimental wavefronts (lower right); when the Station 1 wavefronts (upper right) are added to the computed wavefronts, the comparison is even better (lower left) [Ref. 2].

Based on the good agreement with the predicted aero-optic characteristics for the AEDC shear-layer and the measured wavefronts, it was clear that the most controversial assumption within the weakly compressible model was the setting aside of the Strong Reynolds Analogy. As such, in the last AFOSR grant a compressible shear layer facility was designed and constructed at Notre Dame to reproduce the shear layer at AEDC and used to validate the presence of pressure wells within the coherent structures in the shear layer. Figure 4 shows a flow visualization and measured pressure well within a coherent structure in a shear layer matching the AEDC conditions. Figure 4 may be compared to the weakly compressible model predictions in Figure 2. [15]

As a final comment regarding the aero-optic environment associated with the flow around an airborne beam director, it is clear that the most degrading flow environment is due to separated flows. Referring to the Station 1 data in Figure 1, a turbulent boundary layer does induce aberrations on a laser passing through it; however, these aberrations are relatively small compared to that induced by propagation through a free shear layer. Although the OPD_{rms} for propagation through a turbulent boundary layer is relatively low, it should be kept in mind that from time to time the instantaneous Strehl ratio (Eq. 2-1) can drop to near zero. Thus while the average Strehl ratio is high, some applications, such as free-space communication, may need to be concerned with turbulent boundary layers.

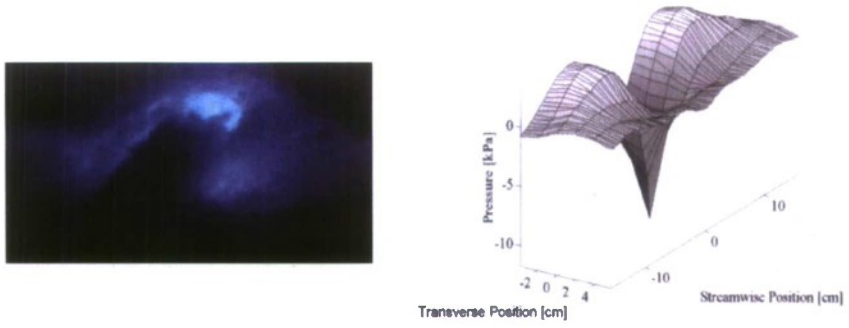

Figure 4. Experimental validation of the Weakly Compressible Model [Ref. 15].

Flow-Control, Feed-Forward Adaptive-Optic Foundations. Having now a physical explanation for the aberrating effects due to propagation through a free shear layer, it is possible to contemplate flow control approaches to mitigating its aero-optical effects. In fact, several Air Force Programs are presently investigating flow control influences on aero-optic environments. Many of these are specifically directed toward attempting to suppress the formation of large coherent structures in a shear layer by the introduction of smaller-scale disturbances into the shear layer near its separation point. On the other hand, Notre Dame has long advocated the use of flow control to regularize the shear layer in such a way that its aberrating structures become "regular" and predictable so that feed-forward approaches to adaptive-optic corrections become tenable. It is well known that free shear layers are receptive to forcing at the separation point; Reference 4 is a review article on the topic. Based on the information contained therein, the most efficient approach is to force a shear layer is at its most unstable frequency and this is the approach taken for the heated jet demonstration reported below. More recent results have shown that forcing can stabilize a shear layer over some distance [16] (recall from the *Introduction* that Notre Dame inferred that stabilization meant regularization). In addition, the more recent literature describes other characteristics of the forced shear layer that can influence the choice of forcing frequency. Figure 5 demonstrates that a shear layer can be caused to stay at the same thickness, that is to say, stabilize its thickness, and that the choice of forcing frequency controls the location where the shear layer's thickness is stabilized; these experiments were performed for relatively high Reynolds number shear layers, albeit for low Mach numbers. As shown in Figure 5, the lower forcing frequencies cause the shear layer to be controlled to farther-downstream distances. This fact will be returned to when discussing our forcing experiments for the compressible shear layer. While the literature did not suggest that the shear layer became "regularized" in the sense that every structure convecting through this region is identical and its passage is periodic, the fact that the coherent structure size is related to the shear layer thickness implied to us that regularization was possible. If, indeed, shear layers could become regular and if the aberration patterns had a concomitant regularization, then making flow control part of the adaptive-optic scheme could allow a feed-forward adaptive optic correction that would circumvent the bandwidth limitations imposed by the time delays associated with wavefront sensing, conjugate computation and

application, and any latencies present in the electronics associated with the deformable mirror and its drivers.

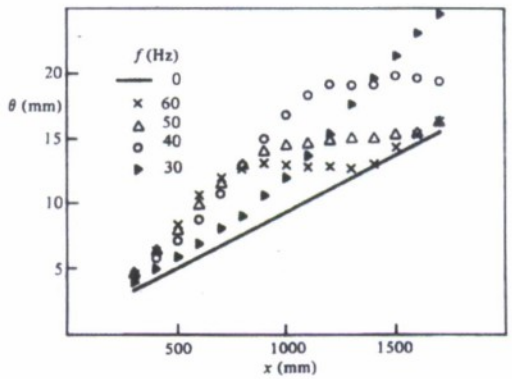

Figure 5. Evidence of the receptivity of a shear layer to forcing by oscillating a trailing edge flap [Ref. 16].

III. FEED-FORWARD DEMONSTRATION

The first accomplishment of this grant was to take advantage of a number of major accomplishments from the previous grant to demonstrate feed-forward adaptive-optic correction of a 19 cm X 10 cm laser beam propagated through a compressible shear layer. Previously developed and demonstrated was the use of voice-coil actuators to robustly force and regularize a Mach 0.78 high-speed-side shear layer. Although more-thoroughly documented in this grant, phase-locked wavefront information, locked to the forcing signal, was used to construct mathematical models for the wavefront patterns being produced by the regularized shear layer. Conjugate wavefronts were then constructed as a function of phase angle and used to determine actuator displacements on Notre Dame's deformable mirror. The final feed-forward adaptive-optic correction was performed by synchronizing the actuator displacements to the forcing signal, the adjustment of amplitude and phase delay being controlled by a man in the loop.

Shear Layer Forcing. In the last grant a new shear layer facility was designed and constructed, as shown in Figure 6. The new design included a new inlet for a wider test section and included a downstream throat to choke the flow and prevent pressure disturbances from the vacuum pumps from propagating into the test section. [17]

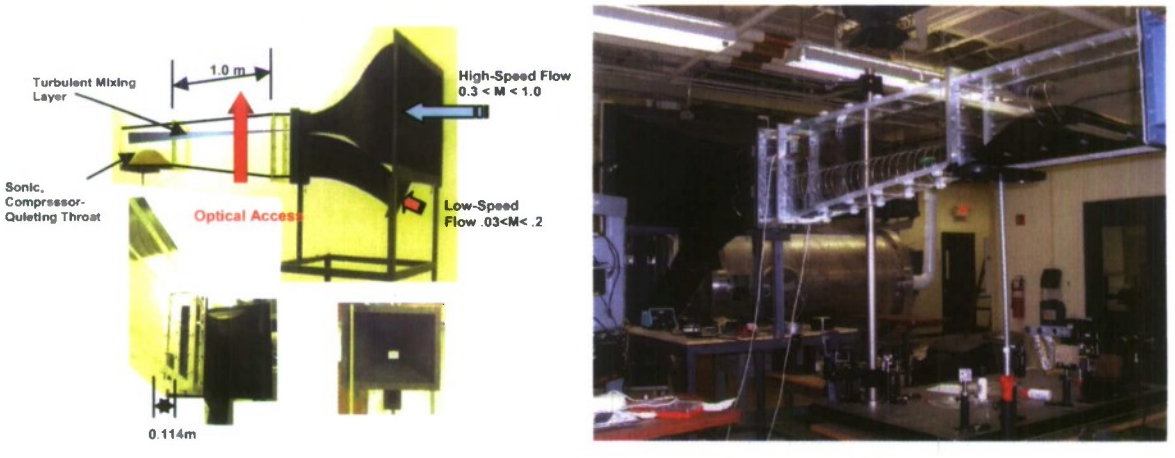

Figure 6. New Compressible Shear Layer Facility [Ref. 21].

Two flow-control actuators were shown to be successful; the most robust actuator type was found to be voice-coil actuators made from 0.3 W speakers cut so that the diaphragm was free to move perpendicular to the flow direction. The amplitude of the motion was as high as 1 mm for the lower frequencies (< 500 Hz) rapidly dropping off with increasing frequency. Figure 7 shows the actuators mounted in the splitter plate.

For much of the wavefront capture and correction experiments a 13.3 cm round beam was used that was slightly clipped to 11.4 cm by the sides of the test section in the cross-stream direction. The captured wavefronts were then extensively analyzed using a proper orthogonal decomposition (POD) analysis. It was found that the majority of the aberration imposed on the beam by the forced shear layer was contained in the first 2 POD Eigen modes. These 2 modes consisted essentially of purely two-dimensional, streamwise-varying aberrations that were periodic with frequencies at the fundamental and first sub-harmonic of the 750 Hz forcing frequency, and could be reproduced to great

accuracy with Notre Dame's deformable mirror (DM). Off-line characterization of the time-averaged DM waveforms allowed the development of a strategy for feeding the waveform forward to the DM to correct the shear-layer abberrated beam. This strategy proved successful the first time it was tried. As noted above, most of the work was performed using a 13.3 cm beam; however, using 750 Hz forcing the beam captured only about half of a wavelength of the aberration such that corrections associated with these beams consisted mostly of tilt correction. More ambitious experiments were performed using a 19 cm beam, again clipped by the facility to 11 cm in the cross-stream direction. Selected frames covering one 750 Hz cycle are shown in Figure 8.

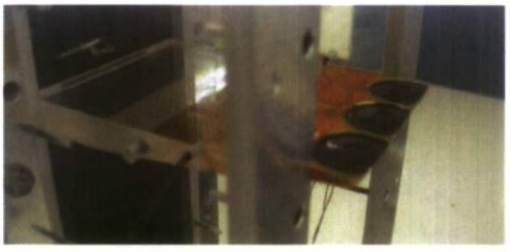

Figure 7. Voice-coil actuators mounted at the edge of the shear-layer splitter plate.

The frames in Figure 8 show only one half of the two-cycle, sub-harmonic repetition of the aberration; the other half of the two-cycle repeat was similar, but sufficiently different so that it required a different conjugate waveform on the DM. In order to correctly phase-lock the order of the two-cycle repeat of the DM waveforms with the shear-layer aberration, a sub-harmonic of 10% amplitude was added to the 750 Hz forcing signal. Details of the entire process are contained in the dissertation of Dr. Dan Duffin [22] and will be forthcoming in a series of papers.

Adaptive-Optic Correction. Once the wavefronts were obtained, conjugates were constructed using the phase-lock-averaged temporal coefficients from the first three eigenmodes for feeding forward to the DM. Then time (phase-angle) series of actuator displacements were constructed for each DM actuator. These displacement phase-angle series were then converted to voltage waveforms and loaded into memory in a waveform generator for each of the 37 DM actuators. The DM was then run and its conjugate waveform measured and compared to the conjugate of the measured wavefronts from the regularized shear layer. One example data series from that demonstration is shown in Figure 9. Figure 9 shows a series of OPD_{rms} wavefront error over an entire cycle of phase angles with the DM running a range of delays from the forcing-signal trigger. As can be seen in the figure, when the mirror is properly phase delayed, the error drops to just over 0.1 μm (240°-270°).

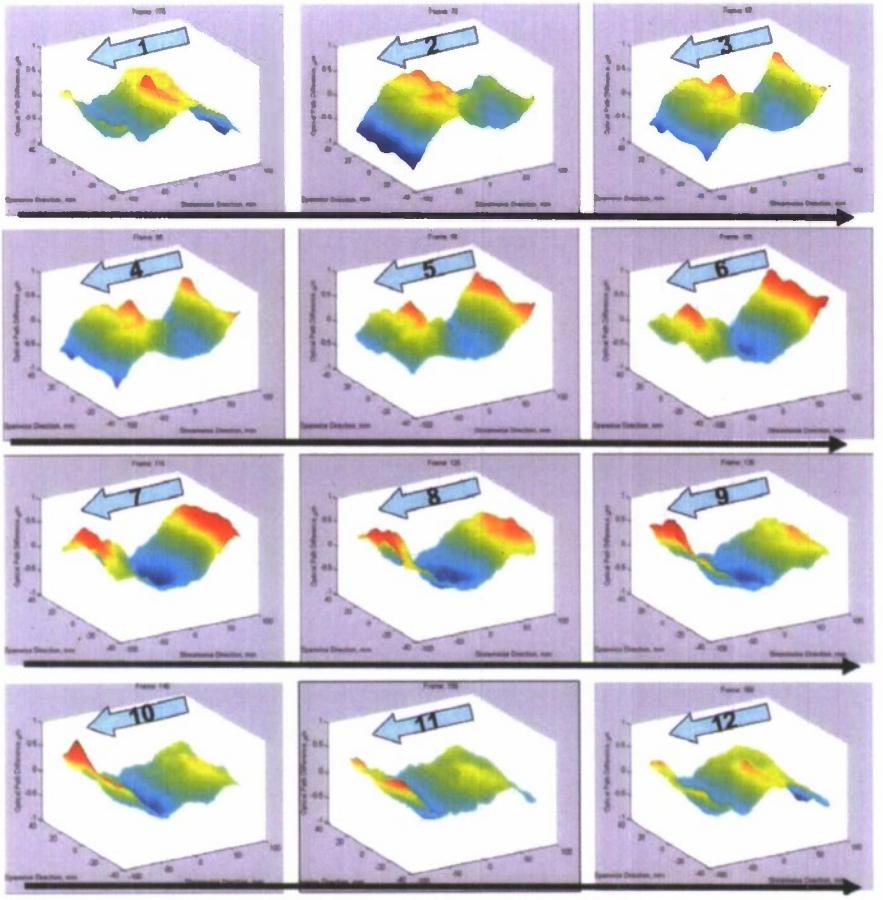

Figure 8. Series of 12 wavefronts spaced by approximately 1.0 X 10^{-4} seconds apart for a 19 cm X 11 cm laser beam propagated through a compressible shear layer (M_{upper} = 0.78, M_{lower} = 0.15) forced by voice-coil-actuators at 750 Hz; the beam was propagated normal to the shear layer and centered at 0.5 m from the splitter plate.

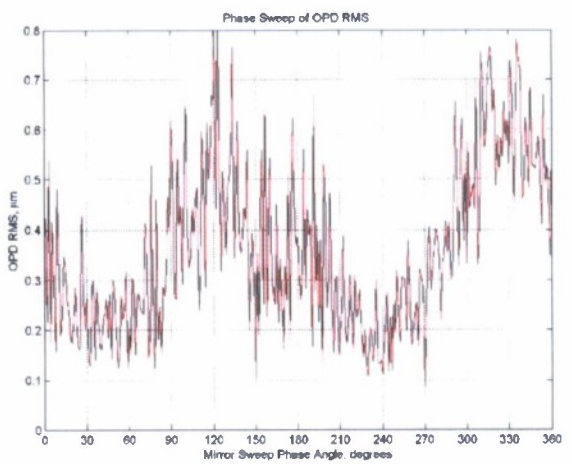

Figure 9. Residual Wavefront Error as a function of deformable-mirror phase delay (10 July 2006).

The Figure 9 data were based on individual wavefronts taken with a phase-locked pulsed laser with a 7 ns pulse length. The Strehl ratio was constructed from far-field reconstructions for a 1 μm laser and the on-axis intensity after tilt removal was divided by the diffraction-limited, on-axis intensity for a 19 cm X 11 cm aperture beam; two selected series of twelve far-field patterns over a range of phase angles, one series for the uncorrected beam and one series for the corrected beam, are shown in Figures 10a and 10b, respectively. The residual OPD_{rms} error in the corrected series was ~ 0.14 μm. Close analysis of the wavefronts and boundary-layer measurements showed that out of this OPD_{rms} residual error, approximately 0.07 of it was due to the turbulent boundary layer on the high-speed wall of the tunnel at the beam-extraction window.

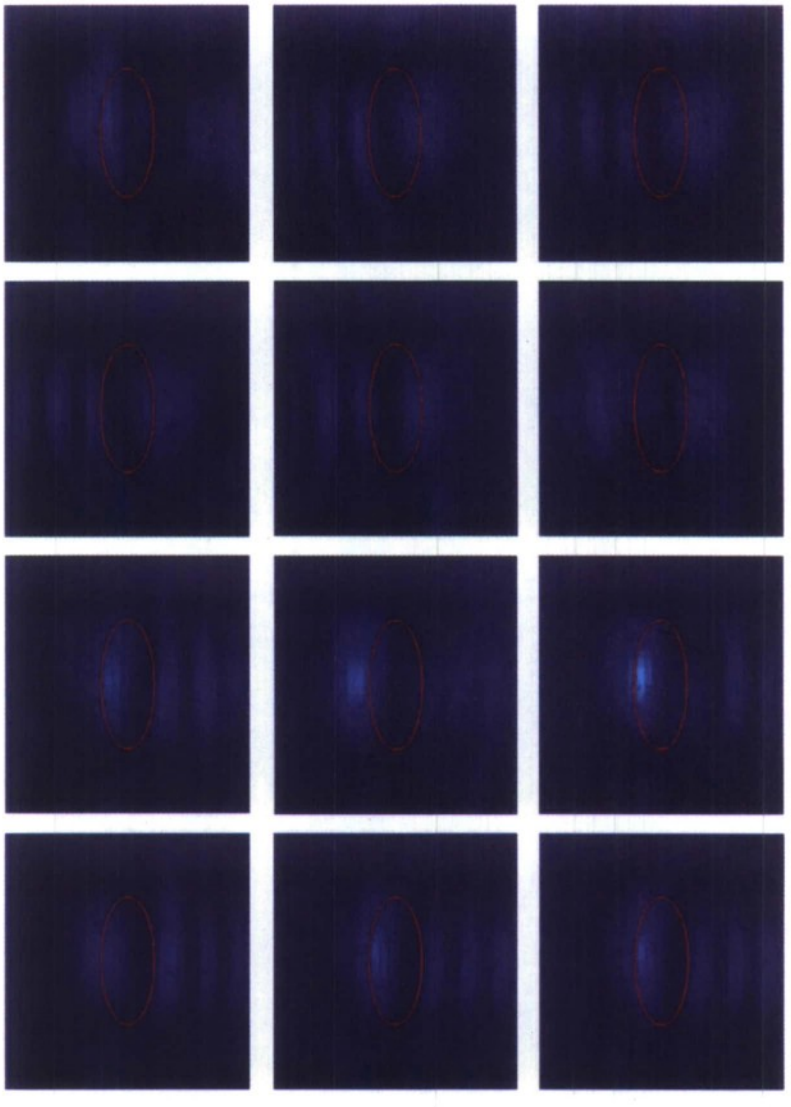

Figure 10a. Uncorrected Far-Field Patterns for a λ = 1.0 μm laser.

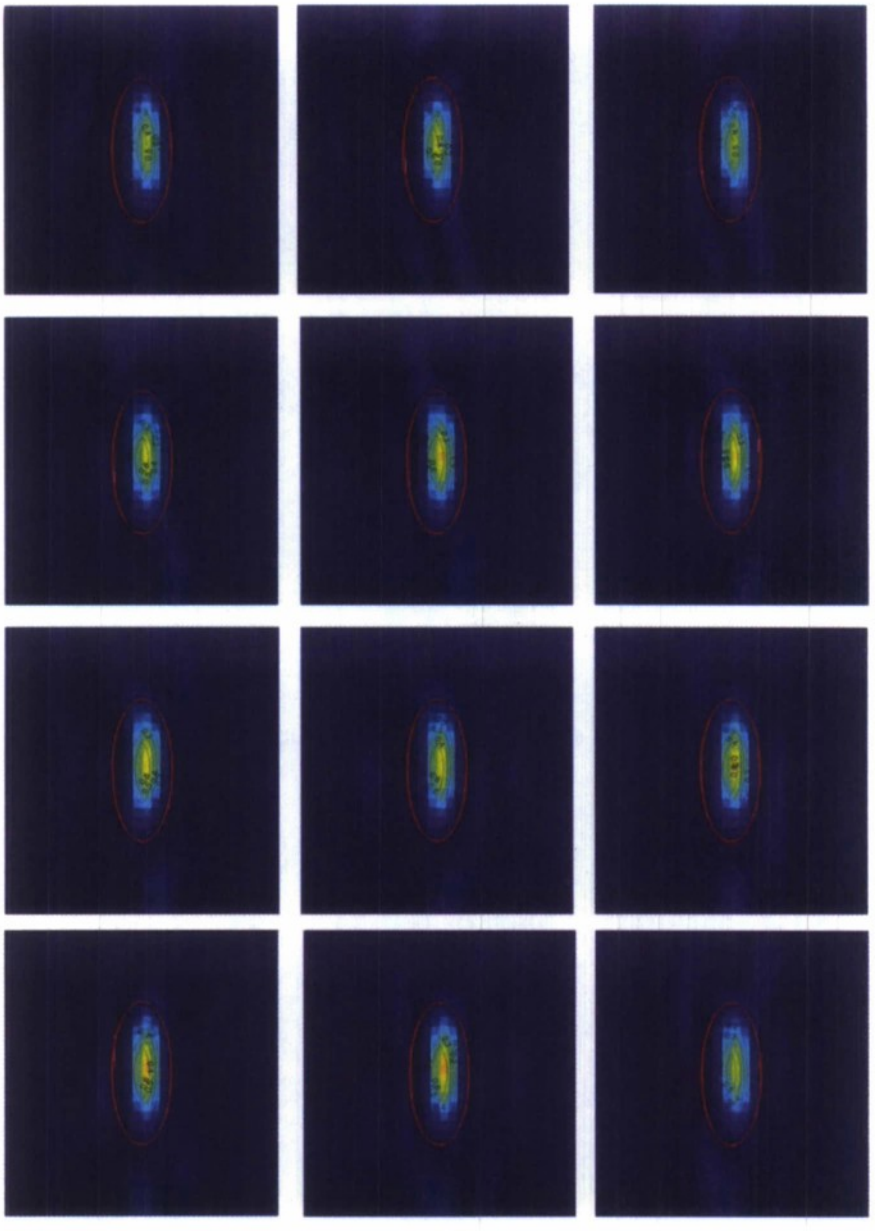

Figure 10b. Corrected Far-Field Patterns for a $\lambda = 1.0$ μm laser.

It should be noted that the aperture was rectangular with the shorter dimension in the cross-stream direction; the result of this aperture is that the diffraction-limited beam becomes elongated as shown in Figure 10b. The diffraction-limited pattern would be a double sinc function elongated in the vertical, cross-stream direction. In Figure 10b, the energy is split into a series of elongated spots which is reminiscent of the aberration being nearly one-dimensional and a sine wave, like a wavy grating.

Figure 11 summarizes the results of the 19 cm X 11 cm correction experiments. Figure 11 shows the dramatic improvement in the far-field irradiance from a Strehl ratio

of ~ 0.14 prior to correction to ~ 0.66 after correction. The final correction to a Strehl ratio of 0.66 represents a reduction in OPD_{rms} from ~ 0.23 μm to ~ 0.1 μm, a reduction of more than 3 dB. When the turbulent boundary-layer contribution is factored in as a root-sum-square contribution, the improved OPD_{rms} drops to below 0.1 μm.

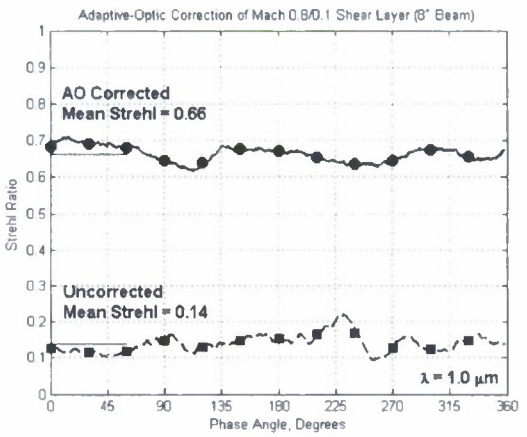

Figure 11. Strehl Ratio for an 8 inch diameter laser beam projected through a Mach 0.8 separated shear layer with and without Notre Dame's Feed-Forward AO approach

IV. AUTOMATED FEEDFORWARD CONTROL SYSTEM

Introduction. The previous section described successful feed-forward experiments that made use of a man in the loop. This section describes work performed under this grant that culminated in the construction of an automated control system that has been demonstrated off line to be able to adjust the amplitude and phase of the DM's conjugate correction. Using the DVM/WCM numerical models discussed in the previous section, it was found that a regularized shear layer imposes nearly sinusoidal aberrations onto a transiting beam with frequencies corresponding to the fundamental and first sub-harmonic of the forcing frequency [22,26]. As described in Section III, this kind of regularization was confirmed in experiments conducted in the University of Notre Dame's compressible shear layer wind tunnel (see Figure 8, for example). In addition to the wavefront measurements shown in Figure 8, measurements have also been made on small-aperture beams that traversed the flow. These small-aperture beam tests showed that, when the shear-layer was unforced, the beam jitter gave an extremely unpredictable signal, but gave a near-periodic, sinusoidal jitter signal when the shear-layer was forced and regularized. This single, essentially sinusoidal jitter signal from a small-aperture beam propagated through the regularized shear layer formed the basis for the AO controller developed under this grant.

Automated AO Controller. The controller design made use of the computational and experimental data showing that the wavefront of a beam transiting a regularized shear layer is essentially sinusoidal with frequency components at the fundamental and sub-harmonic of the forcing frequency [20]. Using this fundamental/sub-harmonic sinusoidal estimate for the aberrated wavefront, a traveling conjugate correcting wavefront was applied to the deformable mirror while amplitude and phase adjustments were performed by the controller. Once the wavefronts become synchronized, the outgoing wavefront aberrations are reduced, thereby increasing the beam's on-target intensity in the far field.

The optical path difference (OPD) associated with the forced shear layer was assumed to be of the form,

$$OPD_{sl}(t,x) = A_{sl}\sin(k_{sl}x - \omega_{sl}t + \phi_{sl}), \tag{4-1}$$

where A_{sl}, k_{sl}, ω_{sl}, and ϕ_{sl} are the amplitude, wave number, angular frequency, and phase of the forced shear layer's resulting optical wavefront. Since the wave number and angular frequency of the shear layer *OPD* are known, the deformable mirror is driven by a waveform with corresponding *OPD* given by

$$OPD_{DM}(t,x) = A_{DM}\sin(k_{sl}x - \omega_{sl}t + \phi_{DM}), \tag{4-2}$$

assuming that the deformable mirror phase sheet can form the desired sinusoidal wave. The variables A_{DM} and ϕ_{DM} in Eq. (4-2) represent the amplitude and phase of the wave traveling across the deformable mirror; these two variables are unknown and optimized via the AO controller. The goal was to use estimates of A_{sl} and ϕ_{sl} to determine the amplitude, A_{DM}, and phase, ϕ_{DM}, of the deformable mirror such that the difference $|OPD_{DM} - OPD_{sl}|$ becomes minimized. This is accomplished using a feedback control system known as a phase-lock-loop (PLL) [23]. The PLL uses an estimate of the phase

difference between the incident wavefront and the deformable mirror to synchronize the phase of the deformable mirror's wavefront with the phase of the incident aberrated wavefront. This approach replaces the need for an array of two-dimensional real-time wavefront measurements (which become bandwidth limited in the case of high-speed aero-optic disturbances) with a single one-dimensional position-sensing device.

AO System Setup. The eventual AO system will consist of a deformable mirror, two small-aperture position-sensing devices, a feed-forward control circuit and a feedback control circuit as shown in Fig. 12. In a future high-speed shear layer experiment, a single small aperture laser beam will provide feedback information to the AO controller while a large aperture beam propagates through the flow and off the deformable mirror applying corrections.

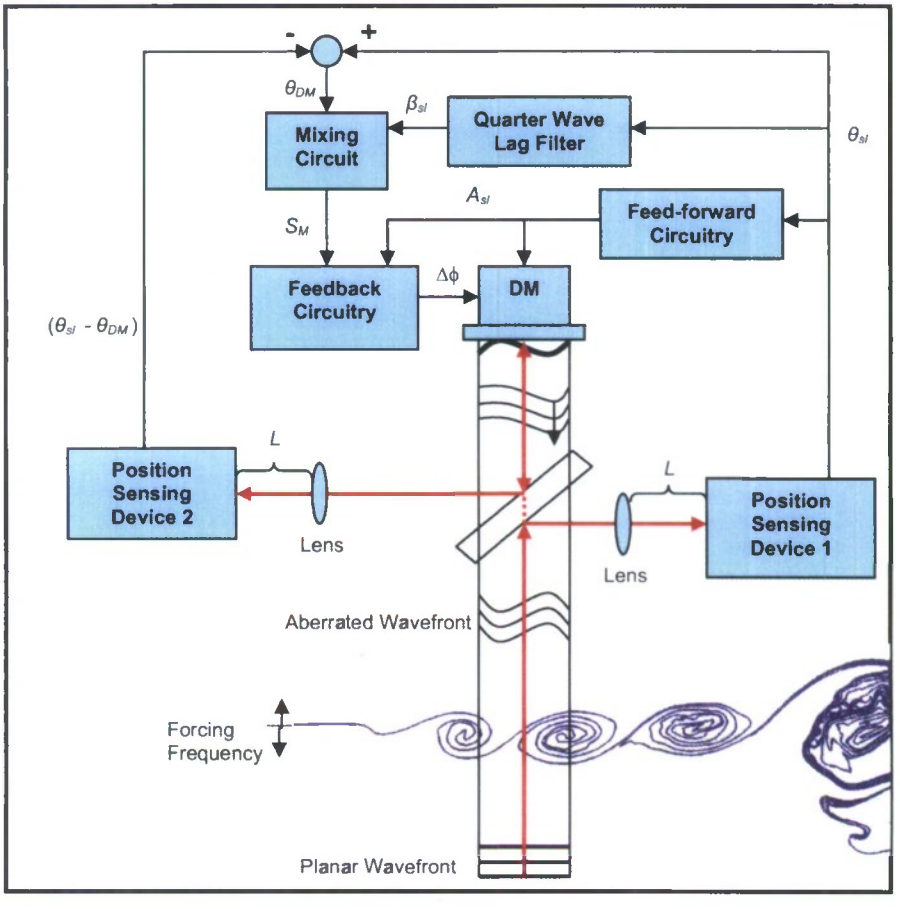

Figure 12. Adaptive-Optic controller and high-speed shear layer experimental setup.

The small aperture laser beam provides a non-intrusive means of gathering feedback information for the controller. In the eventual device, a small aperture beam will be propagated through the regularized shear layer. For the control experiments presented in this report, the jitter signal from this beam was simulated using a function generator. The single beam will then be separated into two beams using a beam splitter. The incident beam will be directed onto the first position sensing device, measuring the time varying

signal due to the aberrating regularized wavefront and appropriately filtered to capture its sinusoidal nature. The filtered signal will then be used as an input into the analog feed-forward circuit that estimates the amplitude of the aberrated wavefront. This signal will also be used in the feedback circuitry to determine the phase difference between wavefronts. The portion of the laser beam which passes through the beam splitter will be reflected off the deformable mirror and redirected by the beam splitter onto another position sensing device and filtered producing a signal equivalent to the shear layer jitter minus the deformable mirror jitter ($\theta_{sl} - \theta_{DM}$). This signal will be subtracted from the shear layer jitter signal to recover the jitter associated with the deformable mirror alone.

Phase-Lock-Loops (PLLs). Phase-lock-loops (PLLs) are one of the most common feedback systems designed and built by engineers. They are used in a variety of applications such as communication and storage devices, radio and television, etc. A PLL adjusts its frequency with the goal of synchronizing itself with a reference source or input signal. The typical PLL consists of a phase detector (PD), loop filter (LF), and voltage-controlled oscillator (VCO). The PD compares the phase of the reference source with the output from the VCO; this may be accomplished using a multiplier (or mixer) along with a low pass filter. The reference source is mixed, or multiplied, with the output signal producing both a sum and a difference signal. When the frequency becomes locked, this results in a harmonic term at twice the input frequency and a D.C. bias term. A low pass filter is used to attenuate the double frequency term, yielding a D.C. error signal proportional to the phase difference between the reference source and the VCO output. The LF filters the error signal and provides a useful design tool for the control engineer to create the desired system tracking response. Second and third order closed loop transfer functions are commonly designed due to their stability and tracking characteristics. Figure 13 shows a block diagram of a typical PLL. The PD is represented by the mixing block and low pass filter combination.

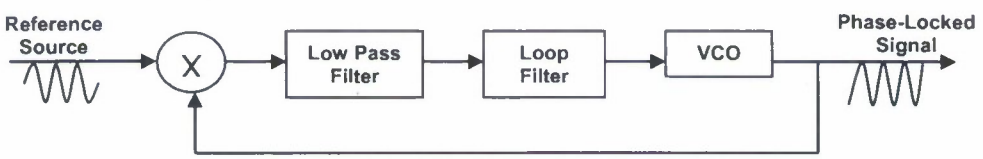

Figure 13. Block diagram of a typical PLL.

In order to apply linear control techniques to the PLL a more conceptual model must be used. Figure 13a shows the block diagram for the linearized PLL model.

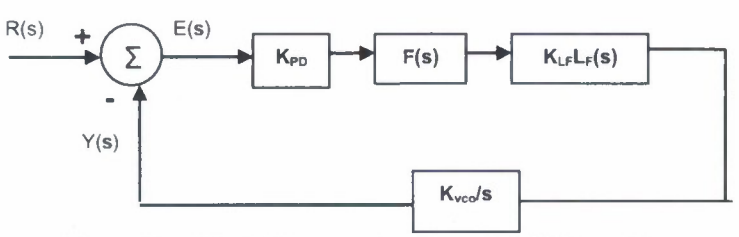

Figure 13a. Block diagram of a conceptual PLL model.

In Figure 13a. a summation bloek is used to represent the mixing funetion of the PD. The output signal (phase-loeking signal), *Y(s)*, is subtraeted from the referenee phase signal, *R(s)*, generating an error signal, *E(s)*. The error is then sealed by K_{PD}, representing the gain magnitude of the phase deteetor and passed through the low pass filter, *F(s)*. The loop funetion, $L_F(s)$, performs any other neeessary filtering aetion while maintaining elosed loop system stability. Finally, the VCO aets as an integrator, where K_{VCO} represents the sensitivity eonstant of the deviee. The elosed loop transfer funetion for the system shown in Fig. 13a. is

$$T(s) = \frac{Y(s)}{R(s)} = \frac{K_{PD}K_{LF}K_{VCO}F(s)L_F(s)}{s + K_{PD}K_{LF}K_{VCO}F(s)L_F(s)}, \tag{4-3}$$

where *F(s)* represents the low pass filter and $L_F(s)$ the funetion designed by the engineer to meet the desired response eharaeteristies. In order to design a system with zero traeking error for both a step input and a ramp input, the elosed loop transfer funetion must eontain two poles at zero (one of whieh is typieally obtained via the VCO) in addition to the low pass filter's left half plane pole. Further analysis reveals that a minimum phase zero must also be ineluded to maintain elosed loop system stability.

Analog Control Circuit Components. In the demonstration system, an analog eontrol eireuit was eonstrueted that eonsists of a PLL eontroller, a feed-forward amplitude estimator, and a series of phase-lag eireuits that produee six additional signals that are ineremen tally phase shifted from the original phase-loeked signal. In the demonstration controller, these seven signals will be used to eontrol the seven rows of aetuators ereating the desired spatial waveform traveling aeross the deformable mirror. This will be modified to produee a single trigger signal for the waveform generator deseribed in Seetion III; however for the purposes of demonstrating the system the seven signals were used to simulate the funetion generator. Figure 14 shows a pieture of the AO eontroller's eireuitry. The following seetion deseribes the method of seleeting the eontrol parameters based on eertain design eriteria.

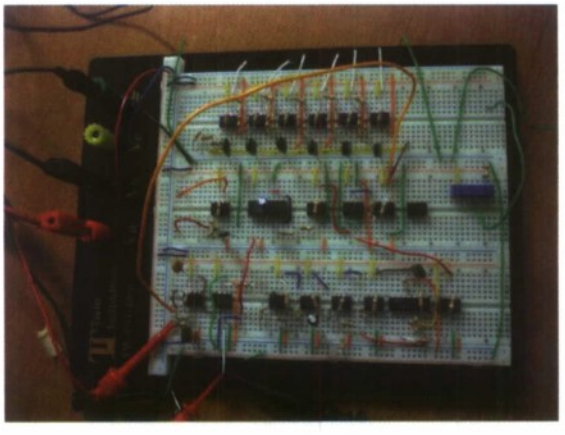

Figure 14. Analog PLL controller test circuitry.

Phase-Lock-Loop Analysis. A PLL control strategy was designed with the goal of synchronizing the deformable mirror's conjugate correction with the regularized wavefront emerging from a forced shear layer. The jitter signal from a small-aperture beam projected through the flow acts as the PLL's reference source used for phase-locking. The response characteristics of the phase-locking process are dependent upon the control parameters used in the control system. A set of design criteria was chosen to aid in the selection of these parameter values. Phase margin, settling time, and the integral of time multiplied by absolute error (ITAE) served as metrics when analyzing the response of the PLL controller.

The two PLL components with design flexibility are the low pass filter and the loop filter; the low pass filter is modeled based upon the expected reference frequency while the loop filter is designed with specific closed-loop response characteristics in mind. In order to achieve an asymptotic response with zero tracking error to both step and ramp changes in phase a second order PLL was employed; a double integrator enables the circuit to track step and ramp changes in phase while a minimum phase zero ensures closed-loop system stability. Therefore, the low pass filter and loop filter Laplace transforms are given by,

$$F(s) = \frac{\omega_p}{s + \omega_p} \tag{4-4}$$

and

$$L_F(s) = \frac{K_{LF}(s + \omega_z)}{s\omega_z}, \tag{4-5}$$

respectively. The Laplace transform representing the VCO is given by

$$V(s) = \frac{K_{VCO}}{s}, \tag{4-6}$$

resulting in an open-loop transfer function,

$$GH(s) = \frac{K_{PD}K_{LF}K_{VCO}(\omega_z + 1)}{s^2 + [(\omega_p)s + 1]} \tag{4-7}$$

and a closed-loop transfer function,

$$T(s) = \frac{K_{PD}K_{LF}K_{VCO}(\omega_z + 1)}{\omega_p s^3 + s^2 + K_{PD}K_{LF}K_{VCO}(\omega_z)s + K_{PD}K_{LF}K_{VCO}} \tag{4-8}$$

derived from Eqn. (4-3).

To simplify the analysis, the open-loop system's pole and zero are assumed to be above and below the unity gain bandwidth (ω_u) by a factor of δ, respectively where

$$\delta = \frac{\omega_u}{\omega_z} = \frac{\omega_p}{\omega_u}. \tag{4-9}$$

Upon substituting Eqn. (4-9) into Eqn. (4-7), the relationship shown in Fig. 15 is obtained where the phase margin is a function of δ: PM(δ). Phase margin is a metric commonly used to quantify system stability; a larger positive value of phase margin is most desirable. It is clear from the plot that as δ increases, the phase margin asymptotically approaches 90 degrees; therefore increasing the value of δ beyond approximately fifteen no longer becomes significantly advantageous.

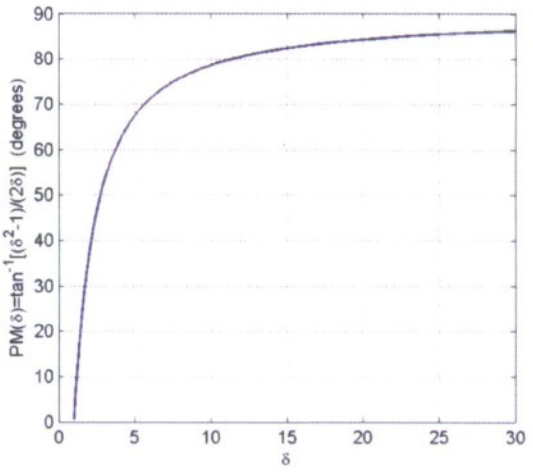

Figure 15. Phase margin as a function of the pole placement factor above the unity gain bandwidth, δ.

The second metric used to analyze the PLL controller was settling time (T_s), defined as the time required for the system's output to remain within a certain percentage of the desired response [24]. Step and ramp response functions were derived from the closed-loop transfer function given in Eqn. (4-8). Figure 15a. shows settling times for a step response (left) and ramp response (right) versus δ for a given set of pole placement values.

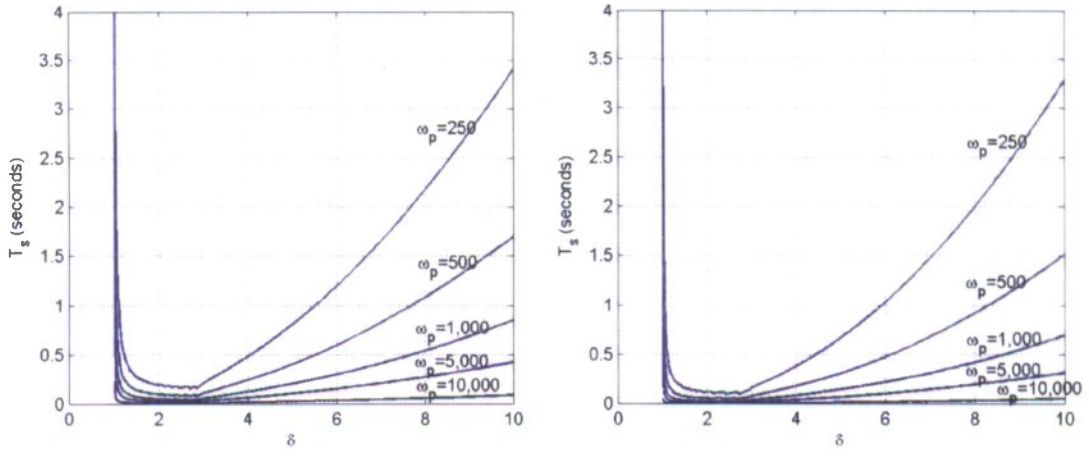

Figure 15a. Settling time versus δ (the pole placement factor above the unity gain bandwidth) for various pole locations given a step (left) and a ramp (right) phase response.

Finally, the ITAE performance index was also used as a metric to analyze the control system. This criterion provides a useful measure of the performance based on the system's error accumulated over time [24]. Figure 16 shows the ITAE performance index plotted as a function of δ.

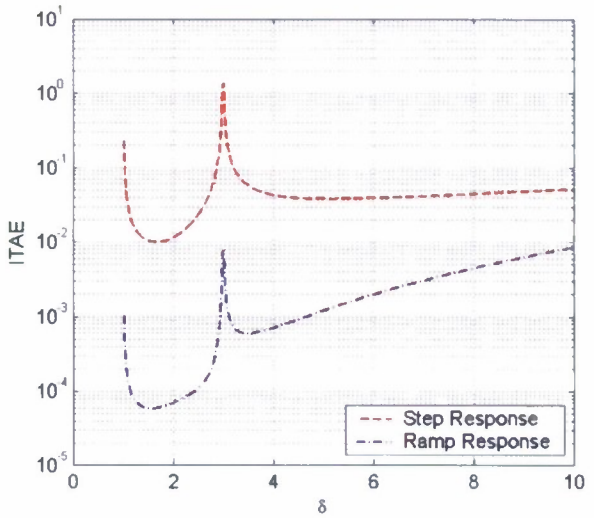

Figure 16. ITAE performance criterion plotted versus δ (the pole placement factor above the unity gain bandwidth) given a step and a ramp phase response.

Recall that the low pass filter design is based upon the expected operating frequency (750 Hz for the experiments documented in this report). This filtering condition along with the three design metrics shown in Figs. 15, 15a., and 16 were used to determine an optimal set of PLL parameters. The controller was designed with a value of approximately 2.35 for the factor δ and 200 for the pole placement, ω_p, corresponding to a low pass filter cutoff frequency of approximately 80 Hz.

The finalized PLL design was then modeled in Matlab and used to simulate the control system response. The DVM/WCM simulation [24] was used to simulate a forced shear layer and its emerging optical wavefront. Figure 16a. shows the phase response along with the calculated Strehl ratio as a function of time for the numerically simulated AO PLL correction.

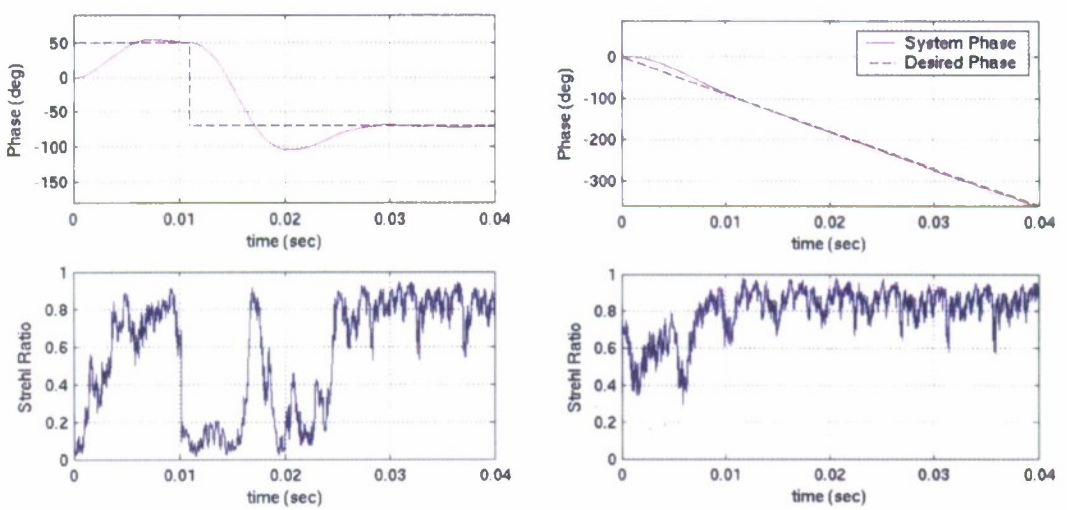

Figure 16a. Phase-locking response of the simulated PLL controller and the corresponding calculated Strehl ratio for a AO correction given a step change in phase (left) and a ramp change in phase (right) between the correcting wavefront and the shear layer's aberrating wavefront.

Finally, the analog PLL controller was constructed by selecting resistor and capacitor values based upon this design analysis. The following section presents experimental results for this alternative AO controller.

Experimental Results. The PLL AO controller described above was tested experimentally using a function generator as a reference source. The controller was designed to operate optimally given a 750 Hz shear layer jitter signal, corresponding to the man-in-the-loop experiment. Therefore, a 750 Hz function generator signal was input into the controller, simulating the jitter signal that will be measured via a small aperture position sensing device in the final alternative AO control experiment. Upon powering the PLL controller, a sinusoidal signal was generated phase-locking to the reference source within seconds. The amplitude of the phase-locked signal also adjusted to match the reference.

Several different experiments were conducted to test the PLL's response characteristics including its amplitude and phase response. Figure 17 shows amplitude error as a function of the time from when the controller was first turned on. It is clear from Fig. 17 that the amplitude of the phase-locking signal asymptotically approaches the reference amplitude, maintaining less than approximately 1 % error within 0.25 seconds. Several more experiments were run in which similar results were obtained. The amplitude of the reference signal was also varied during several tests to ensure the controllers ability to track amplitude variations.

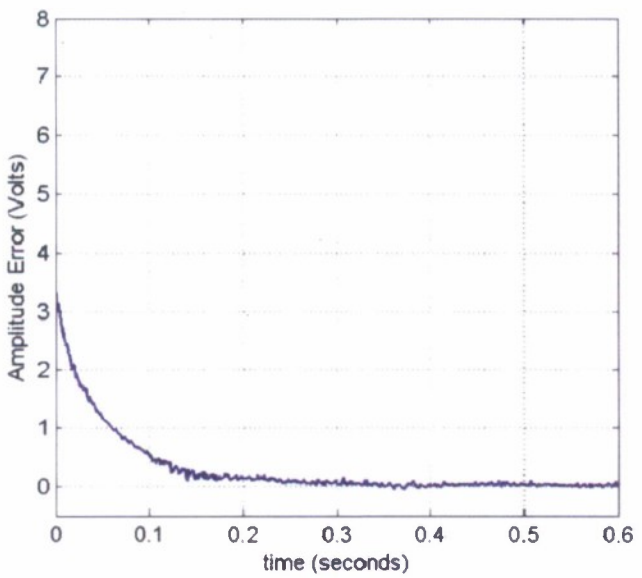

Figure 17. Experimental amplitude error versus time elapsed once PLL controller is turned on given a 750 Hz reference signal with amplitude of 8 Volts.

Additionally, the phase response of the PLL controller was studied. Figure 18 shows the phase error as a function of time for a given test. The controller was able to phase-lock with the reference signal within approximately 1.5 seconds. Several more tests were run demonstrating similar results. The ability of the controller to track step and

ramp changes in phase was studied by varying the phase of the reference signal accordingly during the test. The PLL was able to readjust its frequency and regain phase-locking with the reference source in each case, providing frequency jumps of approximately 10 Hz and less. Further refinement to the PLL circuit will be conducted with the goal of reducing the oscillatory response (increase dampening) and decreasing settling time.

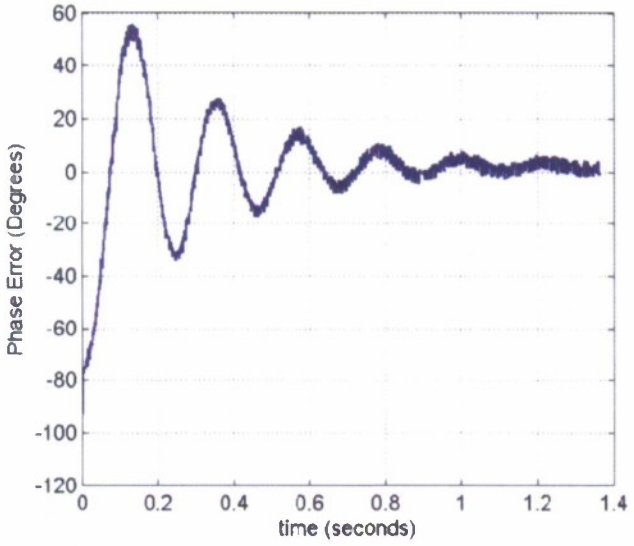

Figure 18. Experimental phase error versus time elapsed once PLL controller is turned on given a 750 Hz reference signal with amplitude of 8 Volts.

The analog controller also contained six phase lag circuits to simulate the function generator described in Section III, which apply consecutive phase shifts to the original phase-locked signal. The resulting seven signals with equally spaced phase shifts are used to construct a two-dimensional traveling waveform. Figure 19 shows three example wavefronts generated from these phase-shifted signals.

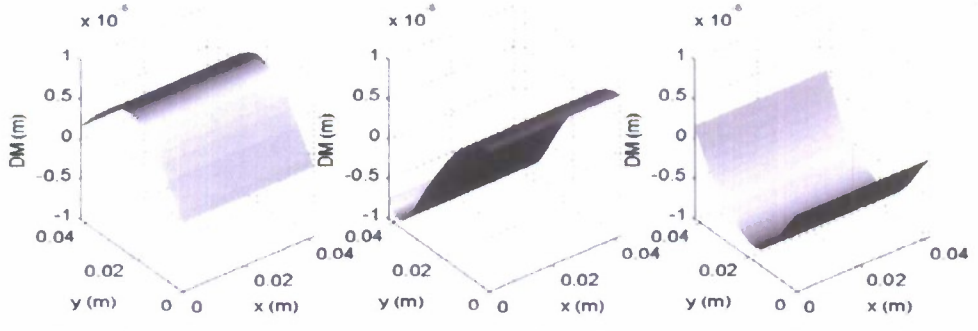

Figure 19. Two-dimensional wavefronts created from the PLLs seven phase-shifted signals (these signals will be used to control the deformable mirror used to perform AO corrections).

A traveling wavefront such as the one depicted above in Fig. 19 (shown in order but widely spaced in phase) will be used to apply conjugate corrections to the DM prior

to integrating the function generator. In the AO correction, the seven signals will control each of the seven rows of actuators used to manipulate the DM as shown in Fig. 20.

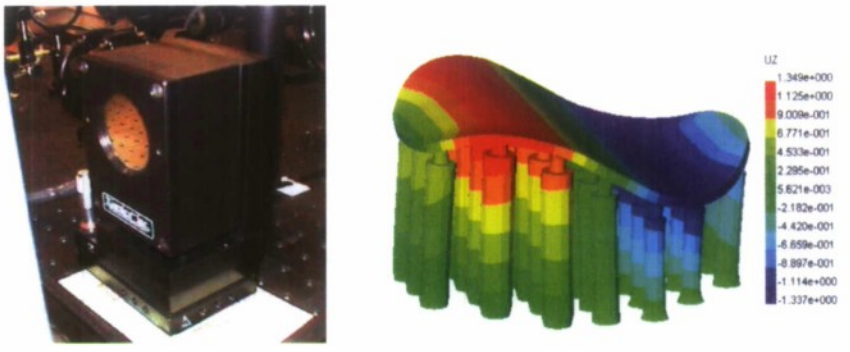

Figure 20. Xinetics DM photograph (left) and 3-D model of mirror and actuators (right).

V. GUIDELINES FOR ADAPTIVE-OPTIC CORRECTIONS BASED ON APERTURE FILTRATION

This seetion is the most lengthy of the report; however, it may be that this information is not generally known and may be if interest to many adaptive-optie system designers. Thus, for eompleteness, a large amount of baekground material is ineluded.

Background Material

Atmospheric Optical Propagation. In past deeades, the study of wavefront error indueed by transmission through air has foeused on the effeets of the free atmosphere. In these studies, "free atmosphere" is defined by a set of assumed eonditions and driving meehanisms. These assumptions allow aspeets of the flow and its optieal effeets to be eharaeterized with a limited number of parameters. Guidelines and rules of thumb for the design of systems for optieal eorreetion based on these eharaeteristies and parameters have been developed and used extensively.

Underlying assumptions. The atmosphere is eommonly deseribed by the Kolmogorov [25] model of turbulenee. In this ineompressible model, energy is transferred from eaeh length seale in the flow to other seales, with a tendeney for the transfer of energy to flow from larger seales to smaller, with large persistent eddies serving as a source of energy for the turbulent flow while viseous effeets at the smallest seales dissipate this energy. It is also assumed that the flow has reaehed an equilibrium state, sueh that the distribution of time-averaged or ensemble-averaged properties is homogeneous and isotropie within a given layer of the atmosphere.

Under these equilibrium eonditions, it is predieted that over the range of seales between that of the large eddies and the viseous dissipation seales, the kinetie energy assoeiated with eaeh length seale in the flow will be distributed sueh that it ean be deseribed as a funetion of the wave number (k) to the negative five-thirds power. The range of seales that ean be eharaeterized in this manner is ealled the inertial range. In discussions and analysis of atmospherie flows and effeets, it is eommon to assume that all aetivity of interest is found in this inertial range, and that the large energy-eontaining seales and small viseous seales ean be ignored.

Obukhov [26] added a deseription of temperature variations to the Kolmogorov model by treating temperature as a passive sealar that would be earried with the flow and be subjeet to diffusion, but would not have any signifieant effeet on the behavior of the flow. In so doing, he found that the distribution of sueh passive sealars eould also be deseribed by a funetion of the form $k^{-5/3}$. Tatarski [7] deseribed the propagation of waves through flows of this nature, assuming that variations in density were the primary souree of effeets on those waves. By the ideal-gas law, variations in density are linked to variations in temperature and pressure in the form

$$\partial\rho = P/(RT)(\partial P/P - \partial T/T). \tag{5-1}$$

However, it is standard praetiee to assume that steep pressure gradients (∂P) dissipate rapidly in sueh flows, and that temperature effeets greatly outweigh the effeets of pressure ($\partial T/T >> \partial P/P$) in the distortion of waves passing through the air.

Parameters of characterization. The spectral distribution of the Kolmogorov model is linked to the idea of a structure function, defined as the average of the square of the difference in some quantity between two points:

$$D_X(x_1, x_2) = \overline{(X(x_1) - X(x_2))^2} . \tag{5-2}$$

In the homogeneous and isotropic flow of Kolmogorov turbulence the location and relative position of the points x_1 and x_2 ceases to matter, and the structure function (D_X), becomes a function of the separation distance (r) between these two points. Over the inertial range in which the $k^{-5/3}$ function serves to describe the spectrum, the structure function can be approximated as

$$D_X(r) = C_X^2 r^{2/3} . \tag{5-3}$$

As noted in the previous section, the effect of such flows on wave propagation is assumed to be caused by density variations linked to temperature variations in the flow. Obukhov indicated that these temperature variations could be described by a structure function of the sort shown in Eqs. (5-2) and (5-3). By the ideal gas law, in this flow where pressure is assumed to be effectively constant, density should be proportional to temperature. Regarding optical waves, it is changes to the index of refraction (n) that are of interest. Over limited ranges of density the change in the index (Δn) will be proportional to the change in density ($\Delta\rho$).[27] Therefore, over the inertial range of length scales, the variations in index of refraction encountered by light waves passing through the flow can be described by the function

$$D_n(r) = C_n^2 r^{2/3} . \tag{5-4}$$

The constant of proportionality in this curve fit, C_n^2, is used widely to characterize the strength of "optical turbulence" in a flow.

Other parameters of characterization tend to be based on C_n^2. Tatarski [7] found that a structure function for variations seen in a wavefront after that wavefront has passed through a flow of this sort could also be described by a structure function, in this case of the form

$$D(r) = 2.91(2\pi/\lambda)^2 r^{5/3} \int_{s_1}^{s_2} C_n^2(s) ds , \tag{5-5}$$

for which s represents the optical path traveled by the wavefront. Using the distribution of wavefront variations described by Eq. (5-5), Fried [28] defined a signal to noise ratio for signals received through a finite aperture. He found that this ratio improved as the aperture was made larger, to gather more of the incoming signal, but he also found that the signal to noise ratio tended to level off once the diameter of the aperture reached a given size (r_0), and that this size corresponded to

$$r_0 = \left(0.423(2\pi/\lambda)^2 r^{5/3} \int_{s_1}^{s_2} C_n^2(s) ds \right)^{-3/5} . \tag{5-6}$$

The length scale r_0 is also known as the coherence length or as the Fried parameter. Other commonly encountered definitions of r_0 indicate that it is the largest size of aperture that can be considered diffraction limited and that it is the size of an aperture over which the mean phase variance will be about one radian. However, the diffraction-limited definition is inherently imprecise, while the phase-variance definition is an

aeeidental side effeet related to a property of apertures that will be addressed in the next section.

Atmospheric optieal distortions are not static. They change as the air and variations in the air causing these distortions move through the optieal path in question with some veloeity (V) perpendieular to that path. The "twinkle" of stars in the sky may be the most eommonly eneountered example of this. Greenwood [30] found the power speetral density of ehanging phase variations seen at a single point eaused by Kolmogorov turbulenee to be

$$PSD_{\varphi} = 0.0326(2\pi/\lambda)^2 f^{-8/3} \int_{s_1}^{s_2} C_n^2(s)|V(s)|^{5/3} ds . \quad (5\text{-}7)$$

It is a property of such speetra that the mean-squared value of the time-varying property ean be found by integration of the speetra over all frequeneies. Greenwood ehose to treat an imagined eorreetive system to deal with these phase variations as a filter which would remove or reduee disturbanees at some frequeneies but have little effeet at others. The residual phase varianee after eorreetion (σ_r^2) would then eorrespond to an integration of the speetrum of Eq. (5-7), after being adjusted by the transfer funetion of this eorreetive filter.

$$\sigma_r^2 = \int_0^{\infty} |1 - H(f)|^2 PSD_{\varphi} = |1 - 1/(1 + i \cdot f / f_C)|^2 \, 0.0326(2\pi/\lambda)^2 f^{-8/3} \int_{s_1}^{s_2} C_n^2(s)|V(s)|^{5/3} ds . \quad (5\text{-}8)$$

The transfer funetion used by Greenwood and shown in the equation above is the transfer funetion associated with a simple RC filter with a eut-off frequeney of f_C. From this, for a desired level of residual phase varianee, one should piek a eut-off frequeney of

$$f_C = \left[0.102(2\pi/\lambda\sigma_r)^2 \int_{s_1}^{s_2} C_n^2(s)|V(s)|^{5/3} ds \right]^{3/5} . \quad (5\text{-}9)$$

As noted earlier, an average phase varianee of about one radian is assoeiated with an aperture of size r_0, and is seen as an aeeeptable level of distortion for many applications. Therefore, it has beeome eommon praetiee to use a value of $\sigma_r = 1$ in Eq. (5-9) and eall the assoeiated frequeney the Greenwood frequeney. (f_G)

Predictions and guidelines for atmospheric optic. In their joint paper on power speetra for eorreetive systems, Fried and Greenwood [29] found that the mean-squared phase varianee over an aperture of diameter D with piston eorreetion (or in an application where mean piston is irrelevant) would be

$$\sigma_{\varphi}^2 = 1.075(D/r_0)^{5/3} . \quad (5\text{-}10)$$

This result is expressed in radians, and is the souree of the association of r_0 with a phase varianee of about one radian. If tip-tilt (T/T) eorreetion of some sort is also applied over the aperture, then the residual phase varianee over the aperture is

$$\sigma_{\varphi}^2 = 0.141(D/r_0)^{5/3} . \quad (5\text{-}11)$$

Higher-order eorreetive systems will generally have multiple points of aetuation within the overall aperture. A eommonly-refereneed rule of thumb for designing suehsystems is that a spaeing of r_s between these points of aetuation will leave a residual phase error of [19]

$$\sigma^2_{r(fit)} = \kappa(D/r_0)^{5/3}. \quad (5\text{-}12)$$

The subscript *r(fit)* is used to indicate that this is a fitting error, caused by the inability of a system with finite degrees of freedom to perfectly match a distorted wavefront. The fitting error constant, κ, depends on the type and shape of correction associated with each actuator. If the actuators only correct for piston in the associated area, then $\kappa \cong 1.26$. For a segmented mirror, $\kappa \cong 0.28$ and for a truly deformable mirror $\kappa \cong 0.23$.

A similar rule exists for residual error due to temporal effects and bandwidth limitations of a system, in terms of the 3-dB cut-off frequency of that system.[19]

$$\sigma^2_{r(temp)} = (f_G / f_{3dB})^{5/3} \quad (5\text{-}13)$$

Likewise, if the system has an inherent time delay of Δt in applying correction, then one may expect a residual phase variance of [31]

$$\sigma^2_{r(\Delta t)} = 28.4(f_G \Delta t)^{5/3}. \quad (5\text{-}14)$$

Aero-optics

The parameters presented in *Atmospheric Propagation Section* have become fundamental to discussions of fluid-optic interaction. Likewise, predictions of performance and guidelines for design of the sort shown at the end of the section have become the standards in crafting systems for correction and compensation. However, these parameters and rules are based upon the assumptions regarding the flow. As is usually the case with simplifying assumptions, these assumptions do not apply to all cases or conditions.

Figure 21 shows a sketch of features that might be found in the flow over a hemispherical object mounted on a flat surface. This could represent a stationary facility in the wind or a turret on a vehicle in motion, up to and including an aircraft in flight. One immediately apparent difference between this flow and the atmospheric case is the fact that that this flow is not homogenous or isotropic. It has clearly identifiable features that are restricted to specific regions of the flow and that have a specific orientation. The line of research in this Grant's effort was specifically directed toward the study of shear layers, such as the one associated with the separation region behind the hemisphere in figure 21. The results presented later have been found to be applicable to a wider range of flows and conditions, but a shear layer will be used as an illustrative example in the following sections.

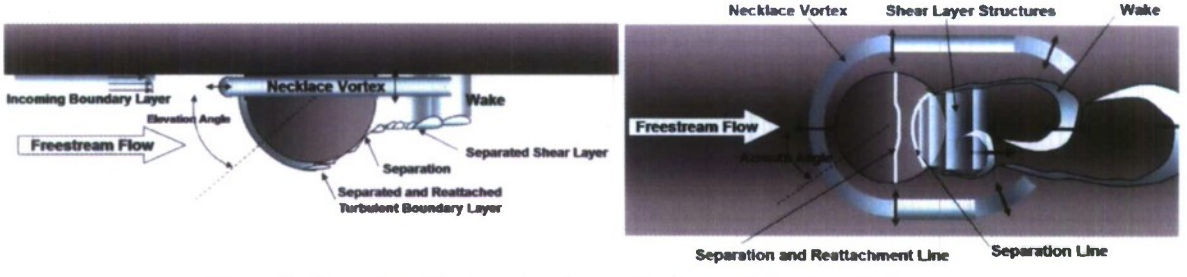

Figure 21. Examples of features in a flow around a hemispherical structure.

Weakly-compressible flows. Shear layers are formed when two neighboring regions in a fluid have mean velocity vectors that are aligned in parallel, but are of different magnitudes, or even pointing in opposite direetions. Shear layers were onee thought to be examples of stochastic turbulencc, with random variations in veloeity imposed on top of the mean veloeity profile, mueh like the model for atmospherie turbulence. However, it was eventually found that large, eoherent struetures are in faet dominant in a developed shear layer.[33] These struetures initially form as growing disturbanees in thc shcar layer "roll up" into vortiees. The shear layer grows in thickness and the associated structures grow in size as fluid from the two flows of differing velocities is entrained into the shear layer and neighboring vortiees interaet and combine in a proeess ealled pairing.[34]

It was once eommon praetiee to assume that fluetuations in statie pressure ($P = P + p'$) were negligible ($p' \cong 0$) within shear layers, even when stream veloeities and relative differenees in velocity were high enough to be eonsidered eompressible flows. As deseribed in the *Introduction* to this report, there are sizable pressure wells inside the coherent, rolled-up structures of a shear layer and these eoupled with the local high-pressure saddle points eause eoneomitant density fluetuations. As diseussed in the *Introduction* and through modeling using the Weakly-Compressible model, thc effeets of these struetures eonveeting through the laser beam introduee reeognizable undulating aberrations on its wavefront.

Spectral characteristics. Not only do flows of this nature have meehanisms of producing distortions not found in the standard atmospheric model (pressure-based as well as temperature-based) but they do not have the speetral eharaeteristies predieted by the Kolmogorov model. To be more precisc, they do not have the same characteristies on the relevant length seales that are normally assumed when using the Kolmogorov model.

In the Kolmogorov model energy is assumed to be added to the flow only at fairly large seales. At this scale, one may find organized, persistent struetures, representing eddies formed by weather systems, plumes from solar heating, or wind passing over major features of the landseape. These elements of the flow are generally assumed to be on sueh a large seale as to have little signifieant effeet on the seale of a reeeiving aperture or the width of a transmitted beam, and that only elements of the flow in the previously mentioned inertial range are of interest.

Referring baek to figure 21, energy is added to thc flow via the interaction between the mean flow and the hemisphere used as an example of a system housing. This produees a variety of energy-containing eddies. If an aperture for thc purpose of receiving or transmitting optieal signals or energy were to exist in this hemisphere, then it is likely that the length seale assoeiated with the flow elements drawn in this figure would be on the same order as the optieal aperture.

As previously noted, this line of research began with a study of shear layers. Figure 22 shows the power speetrum of the defleetion indueed upon a narrow beam passing through a transonie shear layer, eomprised of a Maeh 0.88 stream and a Maeh 0.06 stream. The diameter of this beam was approximately 1 mm, and was direeted through the shear layer at a point 12 em downstream of the point at whieh the two flows first eame into eontaet. A low-pass filter with a eut-off of 18 kHz was applied in taking the measurements to prevent aliasing while a 500 Hz high-pass filter was applied in post-

processing to remove vibration noise. This figure shows that there exists a clear peak frequency around 2.5 kHz.

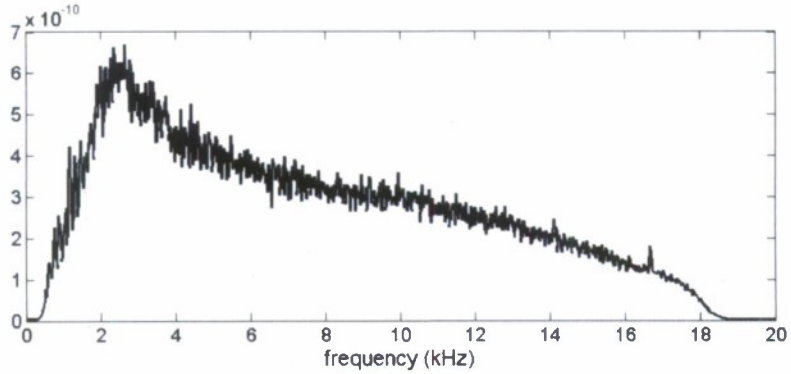

Figure 22. Shear-layer jitter spectrum at 12 cm.

Figure 23 shows several such spectra taken at various streamwise locations. In this figure, each spectrum has been shifted vertically to reflect the location at which the measurement was taken, and all of the spectra have been scaled vertically by the same factor to make features of the spectra visible. Of note in this figure is that the peak frequency associated with each spectrum shifts to lower frequencies with increasing distance downstream.

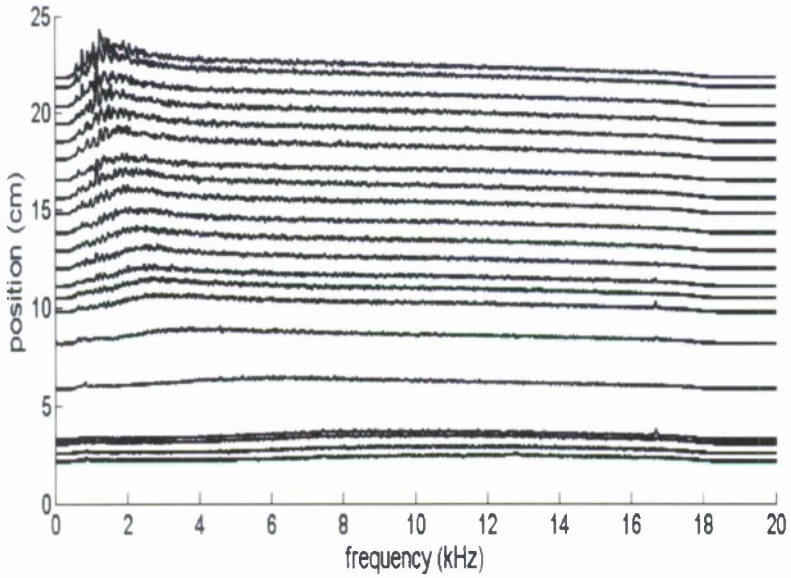

Figure 23. PSD of beam deflection, shifted by position.

Shear layers are dominated by relatively large, coherent structures that initially form from Kelvin-Helmholtz instabilities and grow linearly as the layer develops and moves downstream [33]. The peak frequencies of these spectra correspond to the average size (Λ) of optically-aberrating structures of this nature as they pass the measurement location, and are given by the relationship:

$$f = \Lambda / U_C . \tag{5-15}$$

The convective velocity (U_C) for the spectra shown in Figures 22 and 23 was about 153 m/s. From this relationship and the spectrum shown in figure 22, the average spacing of the structures passing the measurement point of 12 cm would have been about 6 cm from the center of one rolling vortex to the next. Figure 24 shows the structure size estimated by this method at multiple points.

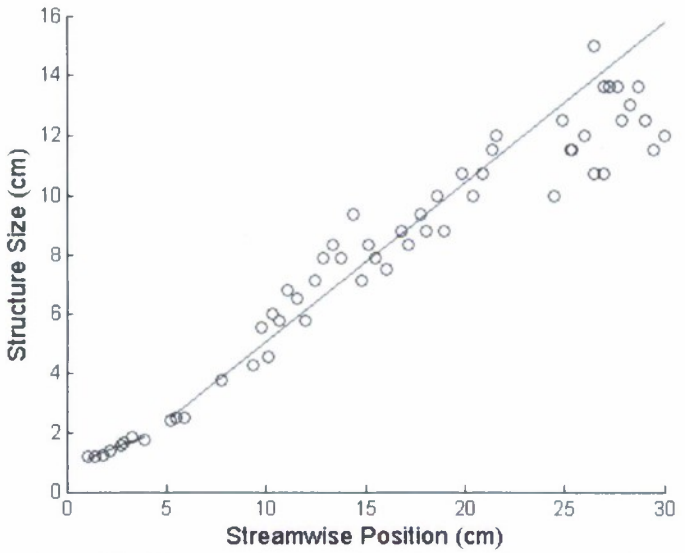

Figure 24. Characteristic structure size and linear growth.

Two features of this figure are of particular importance in comparing this flow to the atmospheric model and the guidelines for correction derived from that model. The first is that the structure size ranges up to about 16 cm over the 30 cm range of locations shown. This indicates that the scale of the shear-layer structures, which contain the highest level of energy in the flow and produce the greatest degree of optical aberration, are not significantly larger than the likely size of the aperture of an optical system, which runs counter to one of the central assumptions for characterizing atmospheric effects. The second is that the length scale associated with these structures grows in size as the shear layer develops and progresses downstream. This also runs counter to the assumptions of Kolmogorov turbulence, in which energy transfer occurs from large scales to smaller. A developed shear layer is effectively a two-dimensional flow, and in such flows energy tends to transfer from small scales to large.[29] Shear layers do eventually become three-dimensional, and thereafter quickly break down in the manner predicted by the Kolmogorov model. However, this may not occur until the structures are far downstream and out of the optical path.

Spectral adjustment via flow control. As mentioned in a previous *Section*, the main thrust of the Grant was to study the use of flow control to regularize the structures causing the aberrations. The structure sizes in figure 24 are estimates of average size, based on the peak frequency of the spectra in figure 23, but the peaks found in those spectra are rather broad. This indicates that the structures and their associated optical aberrations are only quasi-periodic. As detailed in the earlier *Section*, Oster and Wygnanski [36] found that applying forcing, in the form of a moving flap at the initial point of a shear layer where the two streams first come into contact, will force a shear

layer to grow more quickly than it would without such intentional perturbations. They also found that this higher growth rate persists only until it reaches a certain thickness, determined by the frequency of the forcing, and that thickness will remain nearly-constant for some distance down stream until the flow arrives at the location at which that thickness would be reached by the normal, unforced, growth rate. This phenomenon has been further explored and expanded upon,[4, 37, 38] indicating that the period of steady layer thickness also represents a regularization of the rolling vortices in the shear layer, producing a coherent train of structures with greater uniformity in size and spacing.

Work by others at Notre Dame, discussed earlier in this report, has supported this view of shear layer behavior, both computationally,[18] and experimentally .[17, 21] Simulations using the WCM indicate the existence of clear, regular structures and greatly regularized optical distortions associated with those structures. Figure 25 below shows examples of computational results from this model of an unforced and a forced shear layer. Figure 26 shows beam-jitter at a downstream position of 0.415 m in the simulation for the unforced and forced cases, indicating a very close match in form between the sinusoidal forcing and the narrow beam deflection during forcing.

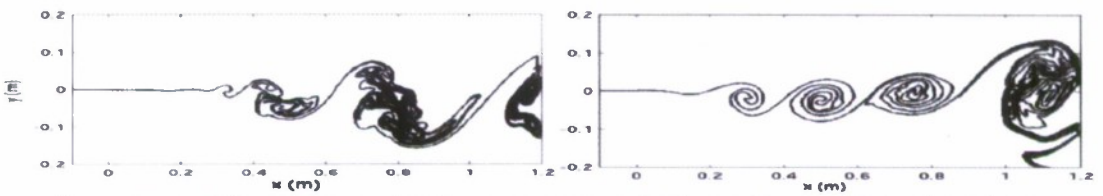

Figure 25. WCM realizations of a shear layer without forcing (left) and with forcing (right). (Nightingale, 2005).[18]

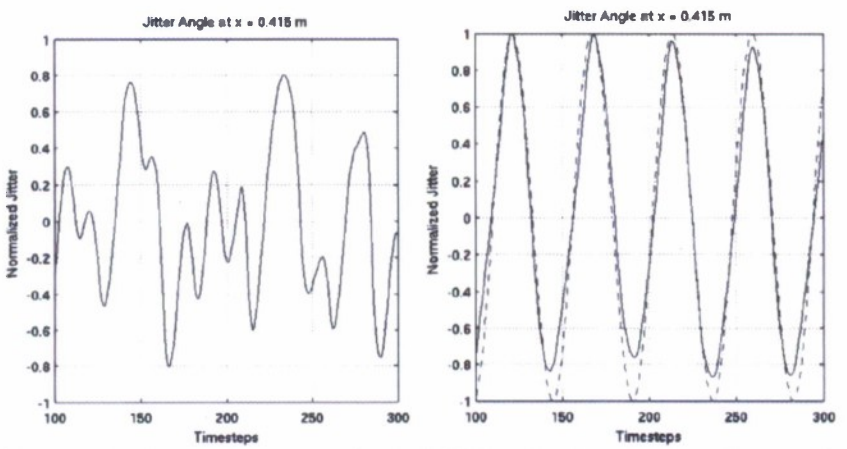

Figure 26. Normalized beam jitter according to WCM realization of a shear layer without forcing (left) and with forcing (right). (Nightingale, 2005).[18]

Figure 27 shows a reconstructed wavefront from optical experimental data taken through a M = 0.78 shear layer being forced at the trailing edge of the splitter plate. While the reconstructed OPL from the experiment is not as close to a pure sine wave as the simulated beam jitter in figure 26, it does show a fairly steady base frequency.

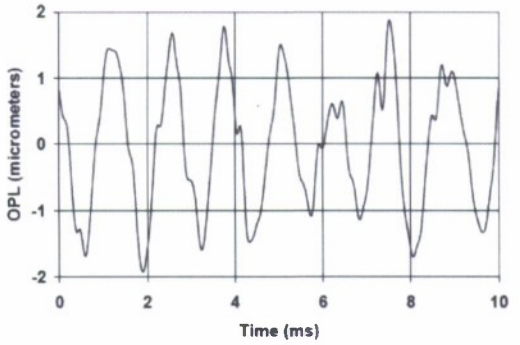

Figure 27. Segment of OPL history for 800 Hz, forced shear layer at x = 570 mm. (Rennie, 2006) [17]

Additionally, research by others at Notre Dame has lead to the successful use of a sinusoidal approximation for real-time optical correction of a forced low-speed heated jet.[22] In light of these results, a sinusoidal approximation of wavefronts is certainly justifiable for shear layers under forcing. Additionally, with Fourier series and power spectra representing optical phenomena as sets of sinusoidal components, there is reason to hope that some of the results found by using this approximation may be applicable to non-regularized flows as well.

Spatial filters

In almost all optical systems the optical information or energy in question is received or directed through a finite aperture. Aberrations induced along the optical path will manifest in different ways, determined by the relation between the length scale of those aberrations, and the size of the aperture.

The effect of a small aperture to negate some forms of wavefront aberrations under the proper circumstances has been known for quite some time. Over 2000 years ago, both Greek and Chinese philosophers documented the principle of a pin-hole in resolving a projected image. Lord Rayleigh developed formulae for the optimal size of a pin-hole to clean up an image for photography.[43] Tyson developed expressions for the "gain" of a deformable mirror removing Zernike modes within an aperture. [35] The following analysis pursues a similar goal, but in a somewhat different manner and will show that this form of analysis can be applied to a wider range of effects and definitions of aberration than Zernike polynomials.

Effects of aperture size on correction. Tip-Tilt (T/T) may be defined as Z-tilt, which is a linear fit to the wavefront itself, or as G-tilt, which is an average of the local gradient at each point on the wavefront. Correcting for G-tilt is best for putting the centroid of the associated far-field pattern on a target point. Correcting for Z-tilt is best for minimizing overall actuator stroke if the corrected wavefront is to be passed on to a higher-order corrective system.

In applying T/T correction to a sinusoidal simulation of a wavefront, an interesting aspect of such correction becomes apparent. Figure 28 shows an example of an aperture in one dimension admitting a sine shaped wavefront. In this instance, the length scale of the variations on the wavefront is larger than the aperture. The portion of the wavefront over this aperture has relatively little curvature, and performing T/T

correction based on Z-tilt leaves a nearly-flat remnant in the aperture, and the resulting far field pattern is close to the diffraction-limited ideal. Figure 29 repeats this example with sinusoidal wavefront aberrations of a length scale smaller than the aperture.

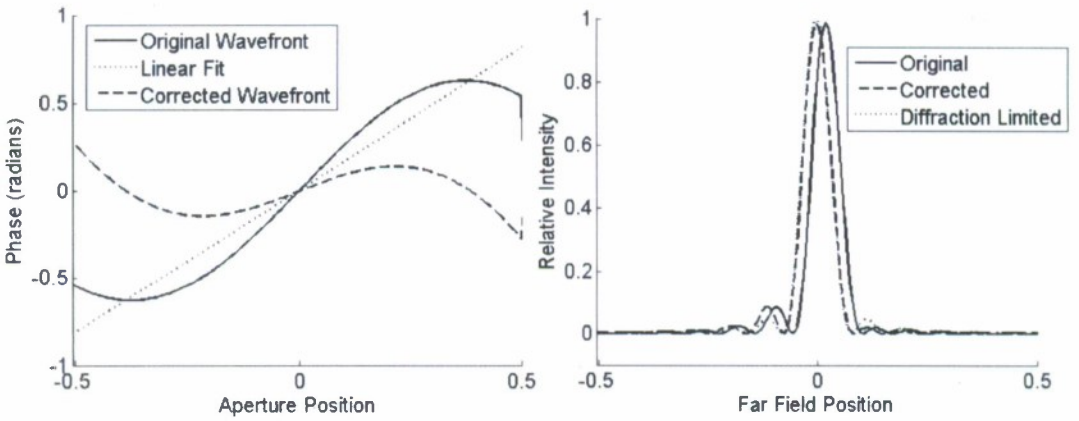

Figure 28. T/T correction for distortions with a long length scale.

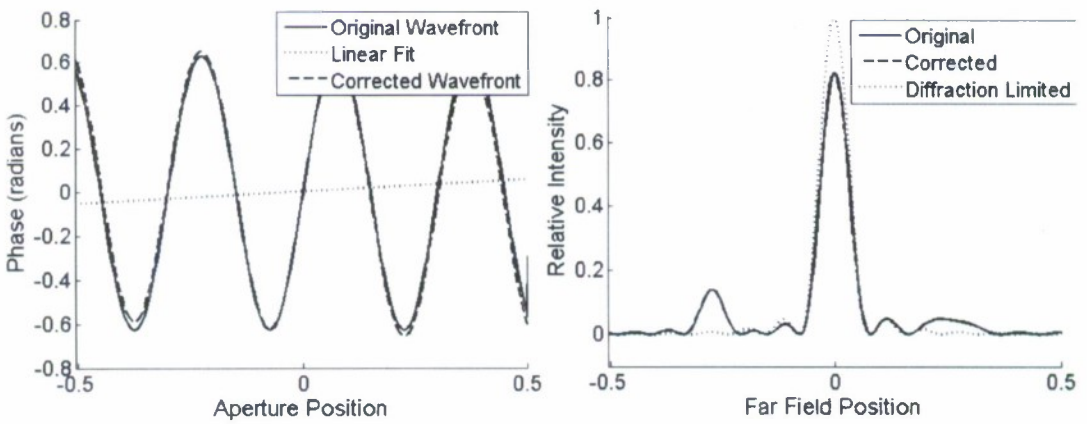

Figure 29. T/T correction for distortions with a short length scale.

Both wavefronts have the same magnitude of aberration, and will have the same average phase variance (σ_ϕ) over time if the source of that aberration is in motion relative to the beam. The uncorrected far field in both cases has Strehl ratio [Eq. (2-1)] of about 0.8. However, effects of T/T correction are quite different for these two cases. In the case with the longer length scale for the disturbance, the overall amplitude of the wavefront aberrations in the aperture is greatly reduced, as the aberration is manifested largely as tilt; as such, the aberration produces in the far field mainly a shifting of the central lobe off of the target point, and providing T/T correction brings the point of highest intensity back in line with the target point where the center of the diffraction limited pattern would be. In the case with a shorter length scale, T/T correction has little effect on the wavefront aberrations, and likewise little effect on the far field.

Filter functions

In this study of aperture effects on correction, we took a slightly different approach to the spatial filter of an aperture than was followed by Tyson. Much as Tyson did, we define a gain function, in terms of a ratio between the average uncorrected aberrations, and the average of the aberrations remaining after correction:

$$G(St_{Ap}) = \frac{\overline{(_{cor}OPD_{rms})^2}}{\overline{(OPD_{rms})^2}}. \tag{5-16}$$

However, while Tyson worked primarily in the frequency domain, we find that working in the time and space domains lead to equivalent results while making it easier to visualize what is going on. The Strouhal number (St_{Ap}) is a non-dimensional ratio used to characterize some types of oscillating flows, and consists of a characteristic frequency, a characteristic length scale, and a characteristic velocity. In this case, the aperture diameter is used as the length scale. Using the relationship shown in Eq. (5-15) this can also be expressed as a ratio between the aperture and the length scale of the disturbance

$$St_{Ap} = \frac{A_p f}{U_C} = \frac{A_p U_C / \Lambda}{U_C} = \frac{A_p}{\Lambda}. \tag{5-17}$$

The Uncorrected Aperture. Finding the gain function of Eq. (5-16) first requires the average aberrations of the uncorrected case to be known. As addressed above, the expected wavefront produced by propagation through a shear layer may be approximated with a sine function. As a frequency response is sought for this effect, it makes sense to do so again

$$OPD(x,t) = K\sin[2\pi(f \cdot t - x/\Lambda)] = K\sin[2\pi(U_C \cdot t - x)/\Lambda]. \tag{5-18}$$

The experimental studies of shear layers that led to this line of inquiry initially dealt with one-dimensional wavefronts, aligned in the direction of the flow. Over such a one-dimensional aperture, the OPD_{rms} at any moment is

$$OPD_{rms}(Ap,t) = \left\{ \frac{1}{Ap} \int_{-Ap/2}^{Ap/2} [OPD(x,t)]^2 \, dx \right\}^{1/2}. \tag{5-19}$$

Inserting Eq. (5-18) into Eq. (5-19) the time-varying $(OPD_{rms})^2$ is found to be

$$\begin{aligned} [OPD_{rms}(A_p,t)]^2 = \frac{K^2}{(4\pi Ap)} \{ & 2\pi Ap - \Lambda\cos[\Lambda^{-1}\pi(A_p - 2U_C t)]\sin[\Lambda^{-1}\pi(A_p - 2U_C t)] \\ & - \Lambda\cos[\Lambda^{-1}\pi(A_p + 2U_C t)]\sin[\Lambda^{-1}\pi(A_p + 2U_C t)] \} \end{aligned} \tag{5-20}$$

A full cycle of the disturbance in Eq. (5-20) occurs over the interval from $t = 0$ to $t = \Lambda/U_C$. Averaging over this period in time will produce the same result that would be approached asymptotically by averaging over increasingly longer periods of time:

$$\overline{[OPD_{rms}(A_p)]^2} = \frac{U_C}{\Lambda} \int_0^{\Lambda/U_C} [OPD_{rms}(A_p,t)]^2 dt = \frac{1}{2}K^2. \tag{5-21}$$

A square or rectangular aperture is virtually identical to a one-dimensional aperture, provided the disturbances are aligned along one of the two axes for the aperture.

However, the same can not be said for a circular aperture. The edge of a circular aperture with a diameter of Ap and centered at $(x,y) = (0,0)$ is defined by

$$y = \pm\sqrt{\frac{Ap^2}{4} - x^2}\ . \tag{5-21}$$

Therefore, integrating over the aperture may be represented by integrating in y to the limits of (5-21) and then over the range from $-Ap/2$ to $Ap/2$ in x. Using Eq. (5-18) to again represent an aberration in the x-direction only, $(OPD_{rms})^2$ at any moment in time proves to be

$$\begin{aligned}\left[OPD_{rms}\left(A_p,t\right)\right]^2 = \frac{4K^2}{\pi A_p^2}\Bigg\{&\frac{\pi A_p^2}{2}\sin^2\left(\frac{\pi U_C t}{\Lambda}\right)\cos^2\left(\frac{\pi U_C t}{\Lambda}\right)\\ &+\frac{A_p\Lambda}{2}\sin^2\left(\frac{\pi U_C t}{\Lambda}\right)\cos^2\left(\frac{\pi U_C t}{\Lambda}\right)J_1\left(\frac{2\pi A_p}{\Lambda}\right)\\ &+\frac{A_p}{2}\cos^4\left(\frac{\pi U_C t}{\Lambda}\right)\left[\pi A_p - \Lambda J_1\left(\frac{2\pi A_p}{\Lambda}\right)\right]\\ &-\frac{A_p}{2}\cos^2\left(\frac{\pi U_C t}{\Lambda}\right)\left[\pi A_p - \Lambda J_1\left(\frac{2\pi A_p}{\Lambda}\right)\right] + \frac{A_p}{8}\left[\pi A_p - \Lambda J_1\left(\frac{2\pi A_p}{\Lambda}\right)\right]\end{aligned} \tag{5-22}$$

in which J_n represents an nth-order Bessel function of the first kind.

As in the one-dimensional case, a full cycle of the disturbance in Eq. (5-22) occurs over the interval from $t = 0$ to $t = \Lambda/U_C$ and averaging over this period in time will produce the same result that would be approached asymptotically by averaging over increasingly longer periods of time. Interestingly, it also leads to the same end result found for the one-dimensional case.

$$\overline{\left[OPD_{rms}(A_p)\right]^2} = \frac{U_C}{\Lambda}\int_0^{\Lambda/U_C}\left[OPD_{rms}(A_p,t)\right]^2 dt = \frac{1}{2}K^2\ . \tag{5-23}$$

One-dimensional T/T correction. For a one-dimensional wavefront in the form of $OPD(x,t)$, observed over an aperture of size Ap, the residual OPD_{rms} over the aperture after T/T removal is:

$$OPD_{rms}(Ap,t) = \left\{\frac{1}{Ap}\int_{-Ap/2}^{Ap/2}\left[OPD(x,t) - \left(A(t) + xB(t)\right)\right]^2 dx\right\}^{1/2}\ . \tag{5-24}$$

where A and B are coefficients defining the tilt and piston being removed. Z-tilt is defined as a linear fit to the wavefront and corresponds to values of A and B that minimize Eq. (5-24). These values can be found by taking the derivative of Eq. (5-24) with respect to these coefficients, which will identify potential minimums at locations where these derivatives equal zero. For this purpose, it is sufficient to do this for just the integral within Eq. (5-24):

$$\frac{\partial}{\partial A}\int_{-Ap/2}^{Ap/2}\left\{OPD(x,t) - \left[A(t) + xB(t)\right]\right\}^2 dx = \int_{-Ap/2}^{Ap/2} -2\left\{OPD(x,t) - \left[A(t) + xB(t)\right]\right\}^2 dx = 0\ , \tag{5-25}$$

$$\frac{\partial}{\partial B}\int_{-Ap/2}^{Ap/2}\{OPD(x,t)-[A(t)+xB(t)]\}^2\,dx=\int_{-Ap/2}^{Ap/2}-2x\{OPD(x,t)-[A(t)+xB(t)]\}^2\,dx=0\,. \quad (5\text{-}26)$$

For a given wavefront, $OPD(x,t)$, this is a set of two equations and two unknowns with the solution:

$$A(t)=\frac{1}{Ap}\int_{-Ap/2}^{Ap/2}OPD(x,t)dx\,, \quad (5\text{-}27)$$

$$B(t)=\frac{12}{Ap^3}\int_{-Ap/2}^{Ap/2}OPD(x,t)dx\,. \quad (5\text{-}28)$$

Using the sinusoidal approximation for $OPD(x,t)$ from Equation (5-18), the minimizing values for A and B are found to be:

$$A(t)=\frac{K\Lambda}{2\pi Ap}\left[\cos\left(\frac{\pi}{\Lambda}(A_p-2U_Ct)\right)-\cos\left(\frac{\pi}{\Lambda}(A_p+2U_Ct)\right)\right], \quad (5\text{-}29)$$

$$B(t)=\pi^{-2}Ap^{-3}\frac{3K\Lambda}{\pi^2Ap^3}\left\{\Lambda\sin\left[\frac{\pi}{\Lambda}(2U_Ct-Ap)\right]+\pi Ap\cos\left[\frac{\pi}{\Lambda}(2U_Ct-Ap)\right]\right. \quad (5\text{-}30)$$
$$\left.-\Lambda\sin\left[\frac{\pi}{\Lambda}(2U_Ct+Ap)\right]+\pi Ap\cos\left[\frac{\pi}{\Lambda}(2U_Ct+Ap)\right]\right\}$$

Inserting these expressions into Eq. (5-24) and averaging over time as was done for the uncorrected case in Eq. (5-21) leads to:

$$\left[{}_{cor}OPD_{rms}(A_p)\right]^2=\frac{K^2}{2\pi^4A_p^4}\left[\pi^4A_p^4-3\Lambda^4-\Lambda^2\pi^2A_p^2+3\Lambda^4\cos^2\left(\frac{\pi A_p}{\Lambda}\right)\right. \quad (5\text{-}31)$$
$$\left.-2\Lambda^2\pi^2A_p^2\cos^2\left(\frac{\pi A_p}{\Lambda}\right)+6\Lambda^3\pi A_p\sin\left(\frac{\pi A_p}{\Lambda}\right)\cos\left(\frac{\pi A_p}{\Lambda}\right)\right]$$

Using the definition of gain from (5-16) and the Strouhal number from Eq. (5-17),

$$G(St_{Ap})=1-\frac{1+2\cos^2(\pi St_{Ap})}{(\pi St_{Ap})^2}+6\frac{\sin(\pi St_{Ap})\cos(\pi St_{Ap})}{(\pi St_{Ap})^3}-3\frac{1-\cos^2(\pi St_{Ap})}{(\pi St_{Ap})^4}\,. \quad (5\text{-}32)$$

This gain function is plotted in figure 30, along with markers to show that the 50% (3-dB) cutoff of this system is found around $St_{Ap}\cong 0.85$.

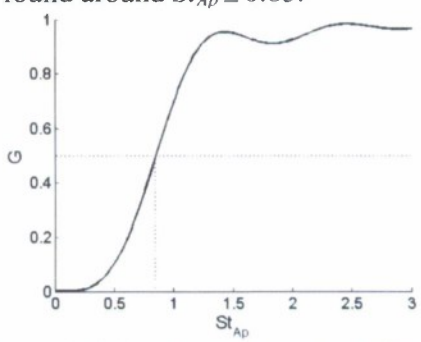

Figure 30. System gain for T/T correction over a one-dimensional aperture.

A common practice in dealing with a filter frequency response or other form of system transfer function is to plot it in log-log scale or decibels against a logarithmic

scale, as had been done for Eq. (5-32) in Figure 31. In this form, it is often easy to see how an otherwise complicated function can be approximated by simpler functions of the form $a(x^b)$ over certain ranges of x. In Figure 31, it is fairly obvious that for values of St_{Ap} greater than the cutoff point, $G(St_{Ap})$ approaches a value of one, or 0 dB, as T/T correction becomes ineffective in dealing with disturbances of a shorter length scale. In this figure it can also be seen that for values of St_{Ap} smaller than the cutoff point, the function has a logarithmic "slope" of 40 dB per decade, indicating that it can be approximated as a function of St_{Ap} to the 4th power.

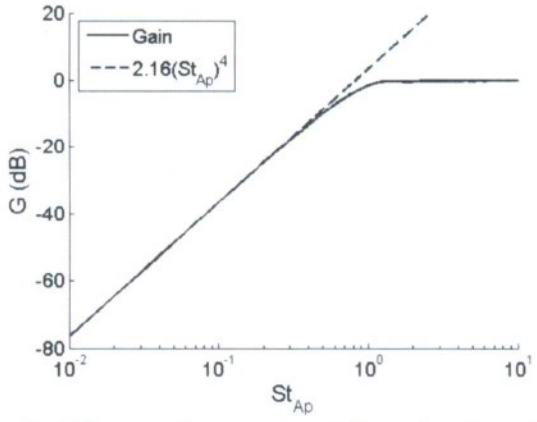

Figure 31. System gain for T/T correction over a one-dimensional aperture, plotted log-scale.

More specifically, a Taylor series expansion of Eq. (5-32), or of the trigonometric functions within that equation, reveals that

$$G(St_{Ap}) \cong \frac{\pi^4 St_{Ap}^4}{45} \cong 2.16 St_{Ap}^4 . \qquad (5\text{-}33)$$

for small values of St_{Ap}.

Two-dimensional T/T correction. As noted, the initial experiments regarding optical distortions caused by shear layers recorded one-dimensional wavefronts aligned with the flow. However, the majority of applications requiring T/T correction involve a beam or optical viewing path with a two-dimensional cross-section, which is often circular. The analysis of the proceeding section for a one-dimensional aperture can be repeated for T/T corrections over a two-dimensional circular aperture, replacing Eq. (5-24) with

$$OPD_{rms}(A_p,t) = \left(\frac{4}{\pi Ap^2} \int_{-Ap/2}^{Ap/2} \int_{-\sqrt{(Ap/2)-x^2}}^{\sqrt{(Ap/2)-x^2}} \{OPD(x,y,t) - [A(t) + xB(t) + yC(t)]\}^2 \, dydx \right)^{1/2} \qquad (5\text{-}34)$$

As with the one-dimensional aperture, the definition of Z-tilt correction is such that the coefficients A, B, and C are set to values that minimize the integral in Eq. (5-34). Using the one-dimensional aberrated wavefront of Eq. (5-17) and performing the same derivations as were done for the one-dimensional aperture leads to the following two-dimensional gain function:

$$G(St_{Ap}) = 1 - \frac{16J_0^2(\pi St_{Ap}) + 4J_1^2(\pi St_{Ap})}{(\pi St_{Ap})^2} + \frac{64J_0(\pi St_{Ap})J_1(\pi St_{Ap})}{(\pi St_{Ap})^3} - \frac{64J_1^2(\pi St_{Ap})}{(\pi St_{Ap})^4}. \quad (5\text{-}35)$$

This two-dimensional gain is plotted in figure 32 and has a 3-dB cut-off at $St_{Ap} \cong 0.93$.

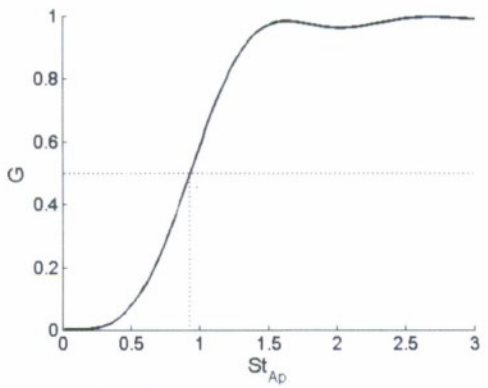

Figure 32. System gain for T/T correction over a two-dimensional aperture.

Plotting the gain in decibels and a Taylor series expansion indicates that the function $G = 1.52(St_{Ap})^4$ serves as an approximation for Eq. (5-35) below the cutoff frequency, Figure 33.

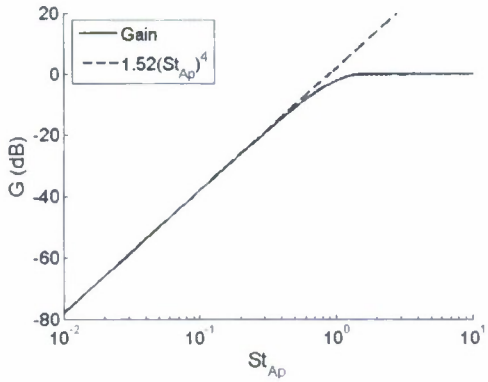

Figure 33. System gain for T/T correction over a two-dimensional aperture, plotted log-scale.

Piston correction. Before pressing onward to other forms of correction, it may be useful to take a step back, and look at correction for piston alone. In addition to cases of active piston correction, there are some applications that are naturally piston-corrected in that piston has no effect on the aspects of interest. This is notably true when resolution or intensity in the far-field is the goal. The far-field intensity pattern produced by a near-field wavefront is unaffected by the average phase or *OPD* of that wavefront. A wavefront of constant phase across an aperture will produce a diffraction-limited pattern in the far field. It does not matter what that phase is, provided it is the same value at all points in the aperture. Only variations in phase and deviations from this mean value have any effect on the far-field pattern. This is one reason why the common approximation for the Strehl ratio,

$$SR \cong \exp\left(-\sigma_\varphi^2\right) = \exp\left[-\left(\frac{2\pi}{\lambda} OPD_{rms}\right)^2\right], \tag{5-36}$$

is known as the large aperture approximation; it assumes that the aperture is larger than the length-scale of the optical distortions. If the length-scale of the distortions is larger than the aperture, then those distortions may manifest partly or even primarily as piston across the aperture.

Therefore, if Strehl ratio or other aspects of the far field intensity pattern are of primary concern, then a wavefront passing through a finite aperture may already be considered piston-corrected, and is subject to the same sort of filtration effect as was seen for T/T correction. The derivation to find the effective gain for piston correction is the same as that for T/T correction, but with the coefficients B and C set to zero. The end results of these derivations are gain functions of

$$G(St_{Ap}) = 1 + \frac{\cos^2\left(\pi St_{Ap}\right) - 1}{\left(\pi St_{Ap}\right)^2}, \tag{5-37}$$

for a one-dimensional aperture and

$$G(St_{Ap}) = 1 - \frac{4J_1^2(\pi St_{Ap})}{(\pi St_{Ap})^2}, \tag{5-38}$$

for a circular aperture.

Both these gain functions are plotted in figure 34. The one-dimensional case has a 50% cutoff of $St_{Ap} \cong 0.45$ and the gain for a circular aperture has its cutoff at $St_{Ap} \cong 0.52$. Also of potential interest are the points at which the functions reach 90%, which are $St_{Ap} \cong 0.74$ for the one-dimensional aperture and $St_{Ap} \cong 0.87$ for the circular. These may be used as an indicator of the beginning of the range for which the large-aperture approximation of (5-36) applies. For that matter, whenever integrating a power spectrum to find the phase variance, as in Equation (5-8), for the purpose of using the phase variance in the large aperture approximation, the spectrum should be filtered with the appropriate piston-correction gain function. The piston-component of wavefront variations has no effect on the far-field pattern or Strehl ratio.

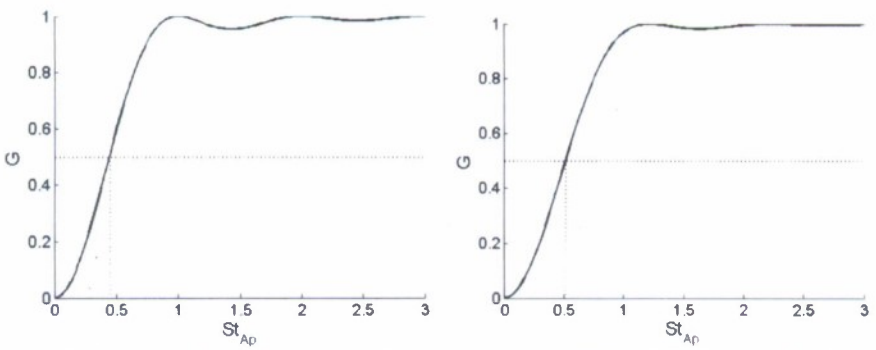

Figure 34. System gain for piston correction over one-dimensional (left) and circular (right) apertures.

The piston-correction gain functions are plotted again in figure 35 in decibel vs. log-scale form, with curves of $G = 3.29(St_{Ap})^2$ and $G = 2.47(St_{Ap})^2$ serving as adequate approximations for these functions below their cutoff values of St_{Ap}.

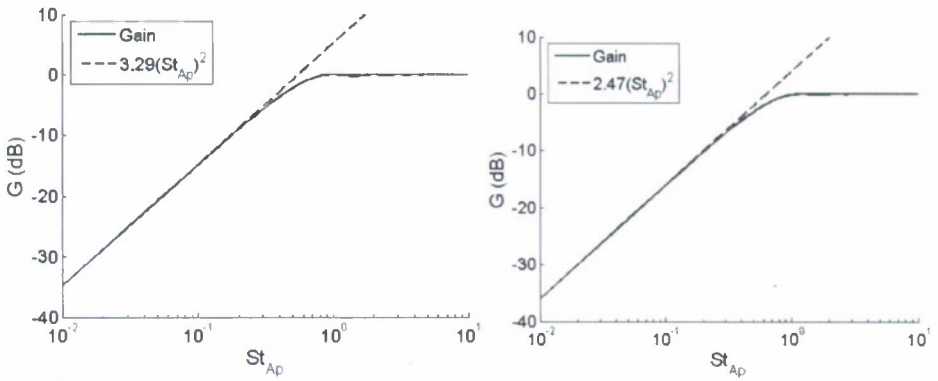

Figure 35. System gain for piston correction over one-dimensional (left) and circular (right) apertures.

G-tilt correction. The analysis in the previous sections parallels that of Tyson and others in describing correction for Zernike polynomials. Piston correction corresponds to the Z_0 polynomial, while T/T correction as defined previous sections corrects both the Z_0 and Z_1 polynomials simultaneously. As noted, Z-tilt is not the only definition of tilt. G-tilt is defined as the average of the local gradients at each point of the wavefront over the aperture, so that

$$G-tilt(t)=\left[\frac{Ap}{2}-\left(-\frac{Ap}{2}\right)\right]^{-1}\int_{-Ap/2}^{Ap/2}-\frac{d}{dx}OPD(x,t)dx=-\frac{1}{Ap}\left[OPD\left(\frac{Ap}{2},t\right)-OPD\left(-\frac{Ap}{2},t\right)\right]. \quad (5\text{-}39)$$

The negative sign inside of the integral in Eq. (5-39) reflects the fact that *OPD* is the conjugate of the wavefront, having equal magnitude (for a medium in which $n \cong 1$) but opposite sign. Correcting G-tilt may make use of Eq. (5-24), as was done for Z-tilt, but for the definition of tilt provided in Eq. (5-39), the coefficient $B(t)$ is selected so that

$$_{corrected}G-tilt(t)=-\frac{1}{Ap}\left[OPD\left(\frac{Ap}{2},t\right)-\frac{Ap}{2}B(t)\right]-\left[OPD\left(-\frac{Ap}{2},t\right)+\frac{Ap}{2}B(t)\right]=0. \quad (5\text{-}40)$$

which leads to

$$B(t)=\frac{1}{Ap}\left[OPD\left(\frac{Ap}{2},t\right)-OPD\left(-\frac{Ap}{2},t\right)\right]. \quad (5\text{-}41)$$

The coefficient $A(t)$ corresponds to piston and has no effect on G-tilt. G-tilt correction is primarily intended to shift the centroid of a far-field pattern to a target point. As noted, average piston has no effect on the far-field pattern. For the sake of comparison with T/T correction in the previous section, $A(t)$ is defined so as to remove the mean piston from the corrected wavefront. The end result of this derivation is a gain function of

$$G(St_{Ap})=\frac{1}{3}\left[4-\cos^2\left(\pi St_{Ap}\right)+6\frac{\sin\left(\pi St_{Ap}\right)\cos\left(\pi St_{Ap}\right)}{\left(\pi St_{Ap}\right)}-9\frac{\left(1-\cos^2\left(\pi St_{Ap}\right)\right)}{\left(\pi St_{Ap}\right)^2}\right]. \quad (5\text{-}42)$$

This gain function is plotted in Figure 36 in both linear and log-decibel scales, and has a 50% cutoff of $St_{Ap} \cong 0.77$. Of particular note is that for $St_{Ap} > 1$, the gain becomes larger than one. This means that when dealing with distortions in the wavefront with a length scale smaller than the aperture, not only is G-tilt correction not effective in lowering the average OPD_{rms} within the aperture, but it may actually increase it, which is likely to

produce a reduction in Strehl ratio according to the large-aperture approximation of Eq. (5-36).

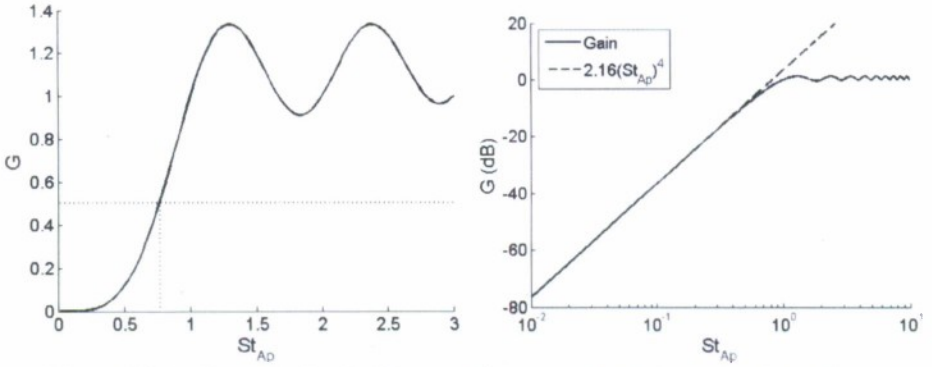

Figure 36. System gain for G-tilt correction over a one-dimensional aperture.

Figure 37 shows an illustration of why this is so. By definition, Z-tilt minimizes OPD_{rms}. Therefore, gain functions based on OPD_{rms} will always be less than or equal to one for Z-tilt correction. However, this is not the definition of G-tilt. Correcting G-tilt for a sinusoidal waveform with a period shorter than the aperture over which the correction is to take place, as shown in Figure 37, may actually induce a significant degree of Z-tilt that was not present and so increase the overall *OPD*. Note that the gain in Figure 36 goes to unity for integer values of St_{Ap} and tends to be greater than one for other values where the disturbance length scale does not divide evenly into the aperture length.

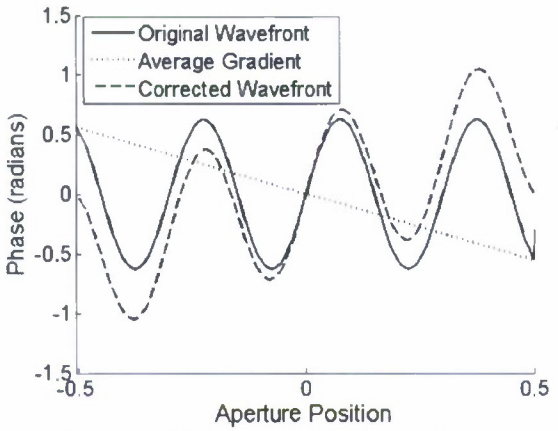

Figure 37. G-tilt correction for $Ap > \Lambda$.

As G-tilt correction moves the centroid of the far-field pattern to a fixed spot, a view of the effects in the far field may also aid in understanding this phenomenon. Figure 38 shows the far-field intensity patterns for the corrected and uncorrected wavefronts of Figure 37. The Fourier-transform-like aspects of far-field propagation cause energy to be transferred from the central lobe to side lobes in this pattern. Shorter length scales of wavefront distortions are associated with side lobes further from the main lobe or intended target point. The way in which the aperture in Figure 37 contains a non-integer number of cycles of the disturbance causes more energy to be transferred to one side than the other. Under such circumstances, the centroid of the pattern is located partway

between the peak of the center lobe and the peak of the large side lobe. Shifting the pattern to put the centroid on the target point actually shifts the main energy-containing lobe of the pattern off of the target point, reducing the intensity at that point.

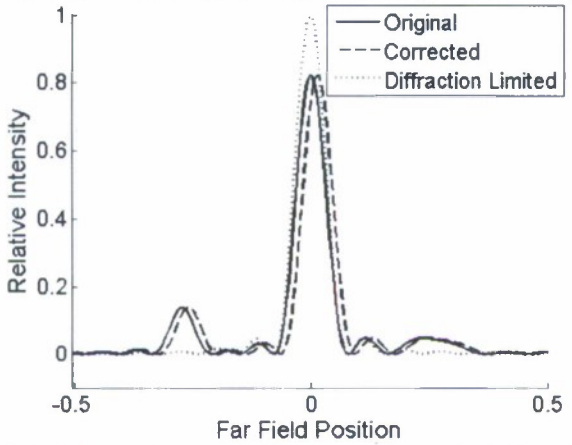

Figure 38. Far-field effects of G-tilt correction for short length scales.

As with Z-tilt, G-tilt correction can also be applied over a circular aperture, with the end result of

$$G(St_{Ap}) = 1 + J_1^2(\pi St_{Ap}) + \frac{8J_0(\pi St_{Ap})J_1(\pi St_{Ap})}{(\pi St_{Ap})} - \frac{20J_1^2(\pi St_{Ap})}{(\pi St_{Ap})^2}. \qquad (5\text{-}43)$$

This gain function is plotted in Figure 39 in both linear and log-decibel scales. It shows the same sort of behavior with higher values of St_{Ap} as was seen for the one-dimensional case, in that it reaches values greater than one. On the other hand, the amplitude of the initial overshoot past $G(St_{Ap}) = 1$ is not as large and the function seems to approach a steady value of $G(St_{Ap}) \cong 1$ more quickly than the one-dimensional case. The 50% cutoff for this function is found at $St_{Ap} \cong 0.88$.

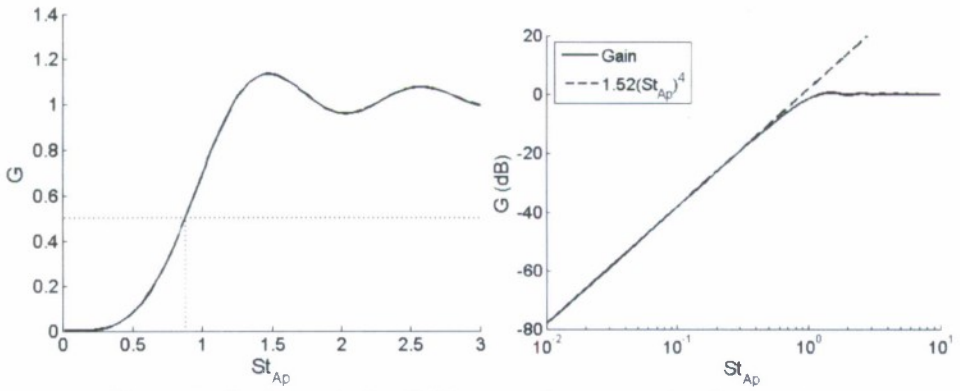

Figure 39. System gain for G-tilt correction over a circular aperture.

Interestingly, the same functions found as Taylor-series approximations for Z-tilt correction across one-dimensional and circular apertures serve as an adequate approximation for G-tilt over roughly the same range. So it would seem that the tendency to equate G-tilt and Z-tilt in many works and applications is not unreasonable,

but only over a range of values in St_{Ap} that corresponds to disturbanees that are primarily T/T in nature.

Periodic correction. Another type of limitation is that of temporal effeets, often eaused by a physieal system having limitations in how quiekly it ean respond to ehanges in eonditions. This often manifests as the system having some upper bandwidth, being unable to eope with eonditions and inputs of a frequeney beyond that. In expressing the eorreetive system gains developed in the preeeding seetions in terms of Strouhal numbers, it would seem that these results inelude temporal effeets, as a Strouhal number eontains a frequeney along with a veloeity and length seale. However, this is merely an artifaet of the relationship between the length seales in the flow and the veloeity with whieh they pass through the optieal aperture. The analytieal and numerieal approaehes used in arriving at these system gains assumed that the eorreetive system was able to instantly reaet to any ehanges in the wavefront and aehieve the best possible eorreetion it eould provide for the system without delay. The effeetive gain so derived refleets the degree to whieh a system with finite degrees of freedom ean mateh the form of the wavefront to be eorreeted.

Periodie eorreetion is eommon in diserete-time systems, in whieh the eorreetion to be applied is updated at intervals. To explore this aspeet of eorreetive systems, the assumption of a sinusoidal wavefront will again be used in the form of

$$OPD(x) = K\sin\left(\frac{2\pi}{\Lambda}x + \varphi\right), \tag{5-44}$$

The time-varying aspeets of Eq. (5-17) have been eombined into the single term φ. If the eorreetion were applied at the point in time eorresponding to φ_0, in the form of a perfeet fit to the wavefront at that moment, then the eorreeted wavefront will have the form

$$_{cor}OPD(x) = K\sin\left(\frac{2\pi}{\Lambda}x + \varphi\right) - K\sin\left(\frac{2\pi}{\Lambda}x + \varphi_0\right). \tag{5-45}$$

In periodie eorreetion there will be some time period, ($\Delta\varphi$) sueh that when $\varphi = \varphi_0 + \Delta\varphi$, the eorreetion will update to mateh the wavefront at that point. Averaging over the aperture, the period of eorreetion, and all possible starting-points for that eorreetion period leads to:

$$\begin{aligned}\overline{(_{cor}OPD_{rms})^2} &= \frac{1}{2\pi}\int_{-\pi}^{\pi}\frac{1}{\Delta\varphi}\int_{\varphi 0}^{\varphi 0+\Delta\varphi}\frac{1}{Ap}\int_{-Ap/2}^{Ap/2}\left[K\sin\left(\frac{2\pi}{\Lambda}x+\varphi\right)-K\sin\left(\frac{2\pi}{\Lambda}x+\varphi_0\right)\right]^2 dx\,d\varphi\,d\varphi_0 \\ &= K^2\frac{\Delta\varphi-\sin(\Delta\varphi)}{\Delta\varphi}\end{aligned} \tag{5-46}$$

The average value of uneorreeted OPD_{rms} remains the same as was found earlier, and the effeetive gain of a eorreetive system of this nature would then be

$$G(\Delta\varphi) = 2\frac{\Delta\varphi-\sin(\Delta\varphi)}{\Delta\varphi}. \tag{5-47}$$

While this derivation was performed for a one-dimensional aperture Eq. (5-47) also represents the result arrived at for a two-dimensional eireular aperture.

In aetually implementing this system, it may be more understandable to express things in terms of the number of eorreetions per eyele of the disturbanees in the wavefront (N_C) or the ratio of the frequeney of eorreetions (f_C) to the frequeney

associated with the wavefront distortions (f_D). Then again, one may begin with only the length of the correction period (τ_1). The relationships between these terms and the characteristics of the flow (U_C and Λ) are

$$\Delta\varphi = \frac{2\pi}{N_C} = 2\pi\frac{f_D}{f_C} = 2\pi\frac{U_C}{f_C\Lambda} = 2\pi\frac{U_C\tau_1}{\Lambda}. \tag{5-48}$$

Figure 40 plots Eq. (5-47) in terms of the number of corrections per cycle. From this figure, it seems that performing only one or two corrections per cycle does not reduce the averaged OPD_{rms} because performing a perfect correction may reduce the OPD to zero at some points in time, but doing so with a frequency this low also allows the distortions in the wavefront to reach a point at which the correction and the distortion are 180° out of phase with each other, doubling the distortion at those times. As the gain functions are expressed in terms of the square of OPD_{rms} to better relate to power spectra, this doubling becomes a quadrupling of the effect, and more than counterbalances the perfect correction performed at the beginning of the cycle.

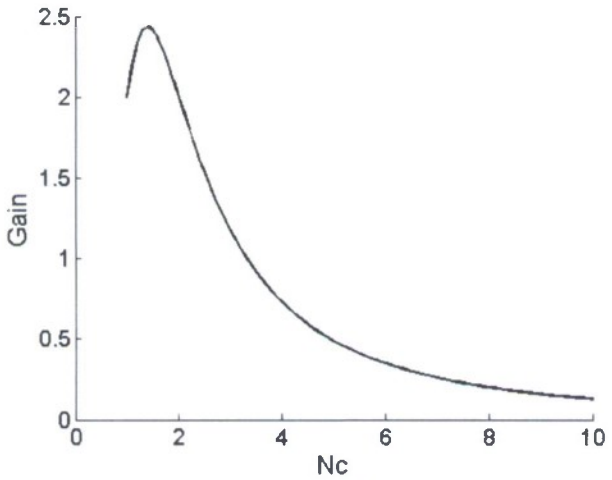

Figure 40. Reduction in wavefront distortions for different frequencies of periodic correction.

From Eq. (5-47) and figure 40 a minimum of 3.3 corrections per cycle is necessary simply to avoid making the average distortion worse, and the 3-dB (50%) point is found at 4.9 corrections per cycle. For small values of $\Delta\varphi$ and corresponding large values of NC, it may be more convenient to use the approximation $\sin(x) \cong x - x^3/6$ to arrive at the following expression

$$G(\Delta\varphi) \cong 2\frac{\Delta\varphi - \Delta\varphi + (\Delta\varphi)^3/6}{\Delta\varphi} = \frac{(\Delta\varphi)^2}{3} = \frac{4}{3}\pi^2\frac{1}{N_C^2}. \tag{5-49}$$

Latency. Latency refers to a delay in applying the correction. This may be caused by the time needed to calculate the appropriate conjugate of the wavefront to be corrected, the time required for actuators to traverse to the required position, or transient effects and delays in control signals reaching the required points and values. Again making use of the sinusoidal wavefront approximation, if the wavefront is of the form Eq. (5-44) and a correction that was a perfect fit but delayed by some time ($\Delta\theta$) were applied, the corrected wavefront would be of the form

$$_{cor}OPD(x) = K\sin\left(\frac{2\pi}{\Lambda}x+\varphi\right) - K\sin\left(\frac{2\pi}{\Lambda}x+\varphi-\Delta\theta\right). \quad (5\text{-}50)$$

Averaging over the aperture and all moments in time during a cycle of the disturbance leads to:

$$G(\Delta\theta) = \frac{2}{K^2}\frac{1}{2\pi}\int_{-\pi}^{\pi}\frac{1}{A_p}\int_{-Ap/2}^{Ap/2}\left[K\sin\left(\frac{2\pi}{\Lambda}x+\varphi\right) - K\sin\left(\frac{2\pi}{\Lambda}x+\varphi-\Delta\theta\right)\right]^2 dx\,d\varphi = 2(1-\cos(\Delta\theta)). \quad (5\text{-}51)$$

As with periodic correction, the results for a circular aperture are the same as for the one-dimensional aperture.

As with periodic correction in the previous section, it is more common to begin with knowledge of the flow and some fixed time delay (τ_2) associated with the system than to know the relative phase. In terms of these factors,

$$\Delta\theta = 2\pi f_D \tau_2 = 2\pi\frac{U_C\tau_2}{\Lambda}. \quad (5\text{-}52)$$

Equation (5-51), plotted in Figure 41, is periodic, as it is based on an assumption of a periodic disturbance. In the case of a periodic or even quasi-periodic disturbance, if a delayed correction is delayed by enough, then it may regain some of its effectiveness by matching and correcting the following cycle of the disturbance. From Eq. (5-51) and figure 41, it seems that performing corrections with a latency phase lag of more than 1.05 radians will add to the OPD_{rms} observed, rather than decrease it. This corresponds to a time lag of about 17% of the time associated with one cycle of the disturbance. However, if the disturbances are truly periodic, then a phase delay of more than 5.23 radians may do some good by catching the next cycle as it comes around.

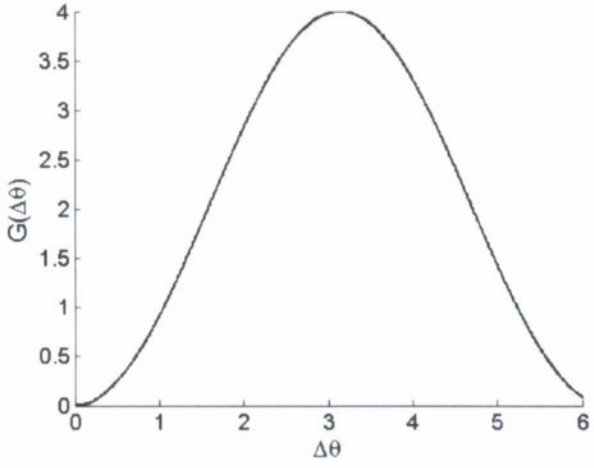

Figure 41. Reduction in wavefront distortions for different degrees of latency in the correction.

If one does not wish to rely on the periodicity of the disturbances, then a phase delay of no more than 0.73 radians is recommended, as this represents a 3-dB cutoff for the system. For latency delays that are relatively small compared to the time scales associated with the wavefront disturbances, it may be more convenient to use the approximation $\cos(x) \cong 1 - x^2/2$ to arrive at the following expression:

$$G(\Delta\theta) \cong 2(1-1+\tfrac{1}{2}(\Delta\theta)^2) = (\Delta\theta)^2. \quad (5\text{-}53)$$

Periodic correction with latency. Virtually any physical system is going to have some latency. Therefore, most systems applying periodic correction will also have latency. Again assuming a sinusoidal wavefront, the corrected wavefront would be of the form

$$OPD(x) = K\sin\left(\frac{2\pi}{\Lambda}x + \varphi\right) - K\sin\left(\frac{2\pi}{\Lambda}x + \varphi_0 - \Delta\theta\right). \tag{5-54}$$

Averaging over the aperture, the period of correction, and all possible starting-points for that correction in the manner of Eq. (5-46) leads to:

$$\begin{aligned} G(\Delta\varphi,\Delta\theta) &= \frac{2}{K^2}\frac{1}{2\pi}\int_{-\pi}^{\pi}\frac{1}{\Delta\varphi}\int_{\varphi_0}^{\varphi_0+\Delta\varphi}\frac{1}{A_p}\int_{-Ap/2}^{Ap/2}\left[K\sin\left(\frac{2\pi}{\Lambda}x + \varphi\right)\right. \\ &\left. - K\sin\left(\frac{2\pi}{\Lambda}x + \varphi_0 - \Delta\theta\right)\right]^2 dx\,d\varphi\,d\varphi_0 \\ &= \frac{2}{\Delta\varphi}\left[\Delta\varphi + \sin(\Delta\theta) - \sin(\Delta\theta)\cos(\Delta\varphi) - \cos(\Delta\theta)\sin(\Delta\varphi)\right] \end{aligned} \tag{5-55}$$

As a check against the results of previous sections, we find that taking the limit of Eq. (5-55) as either $\Delta\varphi$ or $\Delta\theta$ go to zero leads to the expressions for corrective gain with latency or periodicity alone. A potentially useful approximation for delays and correction periods small in comparison to the disturbance cycle is

$$G(\Delta\varphi,\Delta\theta) \cong \frac{1}{3}(\Delta\varphi)^2 + \Delta\varphi\Delta\theta + (\Delta\theta)^2. \tag{5-56}$$

When actually implementing a system, the data available on the characteristics of the disturbances and system are unlikely to be provided in terms of relative phase, as that can only be determined by examining the disturbances and system together and in relation to each other. In practice, it is more likely that one will be confronted with a disturbance that may be characterized by a period of τ_C or frequency of f_C, such that $\tau_C = 1/f_C$. To deal with this disturbance, it is then necessary to select or construct a system that will have a given update period (τ_1) or frequency (f_1) and latency delay (τ_2). The terms of relative phase in (55) and (56) can then be expressed as

$$\Delta\varphi = 2\pi\frac{\tau_1}{\tau_C} = 2\pi\frac{f_C}{f_1} \tag{5-57}$$

and

$$\Delta\theta = 2\pi\frac{\tau_2}{\tau_C}. \tag{5-58}$$

Using these substitutions, Eq. (5-55) may be written as

$$G(\tau_1,\tau_2,\tau_C) = \frac{\tau_C}{\pi\tau_1}\left[\begin{aligned} &2\pi\frac{\tau_1}{\tau_C} + \sin\left(2\pi\frac{\tau_2}{\tau_C}\right) - \sin\left(2\pi\frac{\tau_2}{\tau_C}\right)\cos\left(2\pi\frac{\tau_1}{\tau_C}\right) \\ &- \cos\left(2\pi\frac{\tau_2}{\tau_C}\right)\sin\left(2\pi\frac{\tau_1}{\tau_C}\right) \end{aligned}\right] \tag{5-59}$$

and Eq. (5-56) as

$$G(\tau_1,\tau_2,\tau_C) \cong \frac{4\pi^2}{\tau_C^2}\left[\frac{1}{3}\tau_1^2 + \tau_1\tau_2 + \tau_2^2\right]. \tag{5-60}$$

Application and Verification

The derivations in the previous sections were performed by approximating the wavefronts to be corrected as sine waves. This, in turn, was based on the expected form of distortions produced by a shear layer. However, this is an extreme simplification of a narrow set of flow conditions. Then again, Fourier series, power spectra, and some other forms of analysis are based on the idea that any waveform can be expressed as a summation of sine functions.

Tilt correction in a weakly-compressible shear layer. The gain function for one-dimensional Z-tilt correction found earlier is intended to be compared to a power spectral density. Producing a power spectrum requires a continuous signal or, in the case of discreet data points, a continuous sequence. Producing a spectrum with a significant degree of frequency resolution requires this to be a relatively long sequence. The manner in which wavefronts, as seen through shear layers, were measured in the early stages of Notre Dame's studies is described in detail in other papers.[10, 42] Here, it is sufficient to say that the deflection of a relatively narrow beam at a measurement point was used as an indicator of wavefront slope, much as is done with a Hartman sensor, and then the frozen-flow approximation was used to extrapolate wavefront slopes upstream and downstream of that point at any given time during the period for which data was recorded. A power spectrum for the uncorrected case can be produced by reconstructing a long, continuous wavefront, extrapolated upstream and down from the data recorded. These long, continuous wavefronts may be thought of as being viewed through an infinitely large aperture.

However, this is not possible for the T/T corrected wavefronts as the correction applied will change with each time step, and will change the wavefront accordingly. Thus the corrected wavefront within the aperture at each time step must be considered as a separate case, and can not be simply joined to the ends of wavefronts from previous or following points in time. Because of this, a power spectrum of the corrected wavefront would be limited to what could be produced using only the data points within the aperture at a given time.

Averaging several such spectra from different time steps may be useful in some cases, and tends to produce smoother spectra, but this does nothing to improve the frequency resolution. Achieving higher frequency resolution in such measurements packing a greater number of sensors into the area of measurement, having a higher sampling rate for those sensors, or some combination of the two, depending on the method of wavefront sensing and reconstruction used. However, with any approach the cost or effort of achieving the required number of data points within a finite aperture for a desired resolution may be prohibitive. This degree of resolution was not available at the time of the experiments.

On the other hand, it is possible to record the tilt removed at each time step, as represented by the coefficient B in Eq. (5-24). A power spectrum can then be generated from this long continuous sequence of tilts. As the gain, G, in Eq. (5-32) indicates the degree of aberration remaining after T/T correction, so the function $1 - G$ should correspond to the power spectrum of the aberrations being removed. Figure 42 shows a

power spectrum for beam jitter data taken at a position of 13.4 cm in a shear layer comprised of Mach 0.77 and 0.06 flows. Frequencies below 500 Hz have been filtered out to remove vibrations in the experimental equipment. It also shows the power spectrum for tilt removed in applying T/T correction over an aperture of 5 cm, and the function $1 - G$ scaled in the horizontal axes by the aperture size and the convection velocity of 148 m/s to recover frequencies from the Strouhal number defined in Eq. (5-17). Vertical scales have been normalized by the peak value of the jitter spectrum.

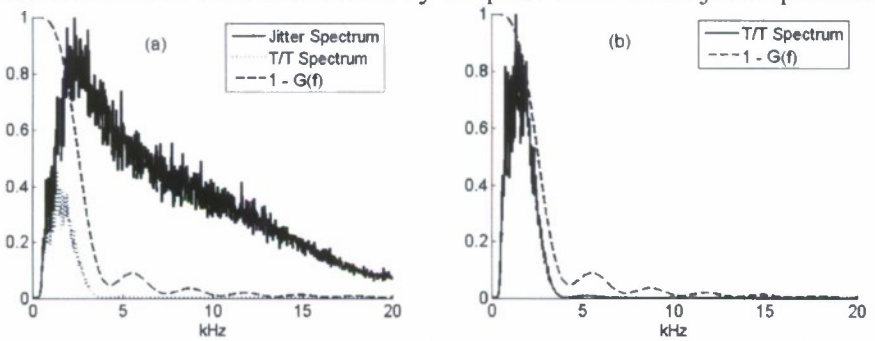

Figure 42. Comparing power spectra for beam jitter, tilt removed, and predicted filter function.

For a more direct comparison, figure 42 (b) shows just the tilt removed spectrum and $1 - G$, with the tilt spectrum scaled by its maximum. The degree to which the prediction of $1 - G$ corresponds with this spectrum can be clearly seen, including the small local maximum seen between 5 and 6 kHz.

Figure 43 (a) shows T/T spectra generated from the same data set used in Figure 42 for three different sizes of aperture. The smaller apertures have more energy associated with them as some elements of the wavefront that could only be corrected with higher-order measures for a 20-cm aperture become T/T effects for apertures of 15 or 10 cm.

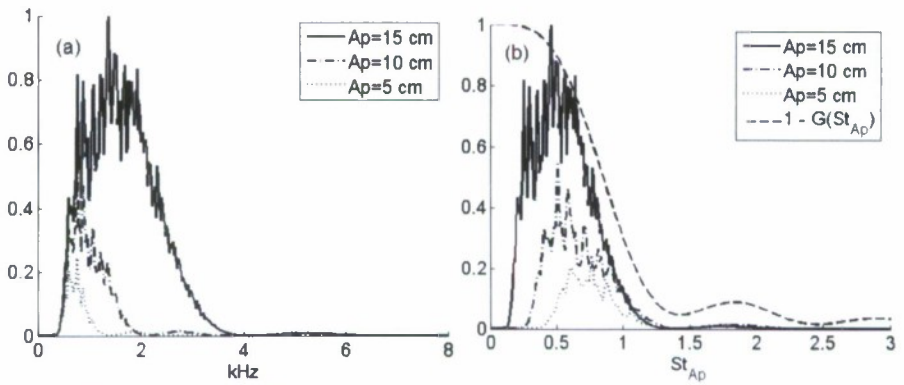

Figure 43. (a) Tilt spectra for different aperture sizes. (b) Scaling tilt spectra by Strouhal number.

Figure 43 (b) shows the same spectra as 43 (a), but plotted against Strouhal number based on the aperture size ($St_{Ap} = Ap \cdot f / U_C$) rather than raw frequency. Also plotted on this figure is the $1 - G$ function for a one-dimensional aperture. One way to interpret this figure is that as Ap decreases, the spectrum being filtered slides to the left and more of the spectrum enters the region for which T/T correction is effective. As with

Figure 42 (b), the way in which the shape of the filter spectrum predicting which frequencies will be removed matches the spectrum for T/T being removed is quite clear.

Periodic correction of a heated jet. In 1996 Cicchiello [39] performed a study of the effects of latency and periodic correction in one-dimensional optical distortions produced by a heated jet. This flow has tendencies towards periodic disturbances and dominating structure sizes similar to those seen in a shear layer, although the mechanism behind the optical distortions produced is the temperature difference between the heated air of the jet and the cooler surrounding air. His results indicated that not only was the Strehl ratio achieved by such correction a function of both the period between corrective updates (τ_1) and the delay in applying the correction (τ_2), but the effects of these factors appeared to be decoupled. That is to say, there appears to exist two independent functions, $h(\tau)$ and $g(\tau)$, such that the Strehl ratio (SR) achieved after correction could be described by

$$SR(\tau_1, \tau_2) = h(\tau_1)g(\tau_2). \tag{5-61}$$

This was based on providing post-processed correction to the wavefronts reconstructed from these measurements with varying correction periods and latency delays, and then constructing the far-field intensity pattern associated with the corrected wavefronts. Figure 44 shows curves of Cicchiello's Strehl ratio results associated with particular values of τ_1 which have been normalized by their value when τ_2 was equal to zero

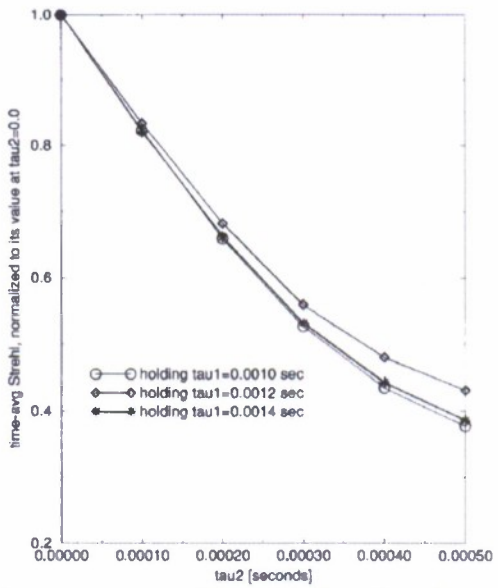

Figure 44. Time-averaged Strehl ratio as a function of time delay between constructing a perfect correction and applying it (τ_2), normalized by the time-averaged Strehl ratio for $\tau_2 = 0.0$ for three values of the period between applying corrections (τ_1). (Cicchiello, 1997)[39]

The manner in which the plotted curves of Figure 44 lie close to each other would seem to support the idea that Eq. (5-61) is an accurate description of the relationship between correction period and latency in determining the Strehl ratio. Particularly striking is the way the results for the most frequent correction rate (τ_1 = 1.0 ms) and the least frequent correction rate (τ_1 = 1.4 ms) lie practically on top of each other.

The corrective gain functions found previously express the ratio of the corrected mean-squared *OPD* or phase variance to the uncorrected case. Ciechiello's results are in terms of Strehl ratio after correction. By the large-aperture approximation Eq. (5-36), Strehl ratios can be related to values of OPD_{rms}, and also to phase variance. Given an average value of $(OPD_{rms})^2$ or σ^2 without correction, the value after correction can be found by multiplying the uncorrected value by the gain function for that form of correction. Therefore, for a disturbance of some period, τ_C, and of amplitude to produce an average uncorrected phase variance of $\sigma_{\varphi 0}$, a plausible prediction for the average Strehl ratio after correction would be

$$SR(\tau_1,\tau_2) \cong \exp(-G(\tau_1,\tau_2,\tau_C)\sigma_{\varphi 0}^2)\,. \tag{5-62}$$

According to Ciechiello's assertion that the effects of τ_1 and τ_2 are decoupled in the form of Eq. (5-61), it should be possible to separate Eq. (5-62) into independent functions of τ_1 and τ_2 so that

$$SR(\tau_1,\tau_2) \cong \exp(-G_1(\tau_1,\tau_C)\sigma_{\varphi 0}^2)\exp(-G_2(\tau_2,\tau_C)\sigma_{\varphi 0}^2)\,. \tag{5-63}$$

which implies

$$G(\tau_1,\tau_2,\tau_C) = G_1(\tau_1,\tau_C) + G_2(\tau_2,\tau_C)\,. \tag{5-64}$$

However, the gain function for periodic and delayed correction Eq. (5-55) found in a previous section does not appear to be separable in this manner. Neither does Eq. (5-56), which is an approximation of Eq. (5-55) for small values of τ_1 and τ_2.

Going back to the paper[39] in which Ciechiello's results were presented, the uncorrected average Strehl ratio associated with his reconstructed wavefronts was 0.265. Using the large-aperture approximation, this indicates an average uncorrected phase variance of $\sigma_{\varphi 0} \cong 1.15$ radians. From time series representations of reconstructed wavefronts associated with this heated jet shown in that paper, a sinusoidal approximation does seem to capture the larger disturbances, which have a period of $\tau_C \cong 0.005$ seconds. Using these values of $\sigma_{\varphi 0}$ and τ_C in Eq. (5-56) and Eq. (5-62) over the same range of values of τ_1 and τ_2 used by Ciechiello, and normalizing the resulting curves in the same manner as was done in Figure 44 produces the set of curves shown in Figure 45, which are presented next to Ciechiello's work for comparison.

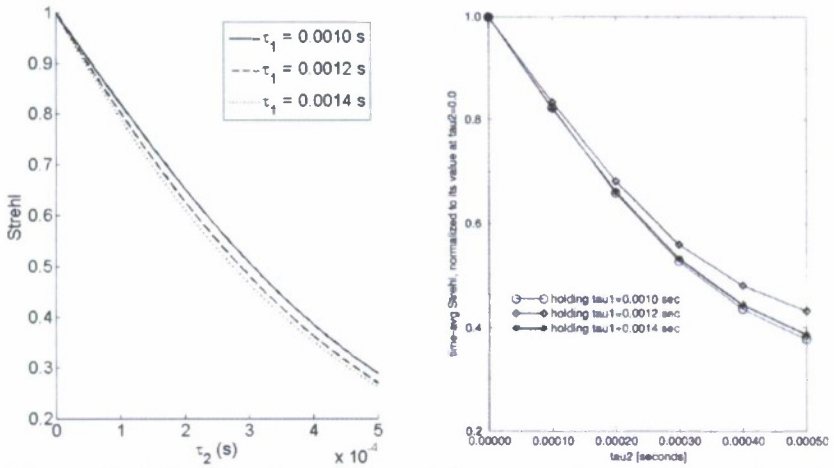

Figure 45. Normalized Strehl ratio predictions (left) compared to experimental results (right).

These simulated and approximated results do match Cicchiello's experimental results quite well. The approximation deviates from the experimental results with greater latency, tending to over-estimate the drop in Strehl ratio. This may be a result of the large-aperture approximation being originally intended for relatively small amplitudes of disturbance and becoming less accurate for larger disturbances, [40] having an error of 10% for Strehl ratios around 0.3. Additionally, while the main structure of the disturbances is of a given size and frequency, there are other components of the distortions that are of differing sizes, and for which given time periods of τ_1 and τ_2 will correspond to different phase periods of $\Delta\varphi$ and $\Delta\theta$ than for the main distortion component. Between these effects and the rough estimates made in producing these curves, it is remarkable how well the approximation agrees with the experimental results.

In light of this, it may be concluded that the gain function for periodic correction with latency predicts the effects of such correction with sufficient accuracy that it may serve as a guideline in designing or selecting such systems for use in a given application.

Tracking. The approximation of a wavefront as a sine wave was intended to capture the dominant qualities of a shear layer and is not one that could be applied to all forms of aberrating flow. However, the filter functions found by this approximation seem to work well in describing the effects and effectiveness of T/T correction on experimental data from shear layers that display optical activity at multiple length scales and associated frequencies. It is worth exploring whether this applies to other forms of optical distortion, such as that from atmospheric propagation and Kolmogorov turbulence described earlier.

As it so happens, this investigation has already been performed, after a fashion, as a byproduct of experiments by other researchers. Boeing, SVS performed a series of tests at the Advanced Concepts Laboratory (ACL) of MIT/Lincoln Laboratory in Lexington, MA, intended to evaluate the effectiveness of various tracking algorithms.[41] This test used a set of moving phase screens to simulate optical turbulence. It should be noted that these screens were constructed with a distribution of phase distortions over a wide range of length scales. As the tracking system was directed at a point source or illuminated target model on the far side of the screens, a scoring laser was passed through the screens along the same optical path. Performance of the tracking algorithms under consideration was evaluated by comparing the output of the tracking control system with the measured deflection of the scoring beam. The authors referred to this as the coherence function, which was defined as

$$\gamma^2_{x\text{-}tr\,x\text{-}sc}(f) = \frac{\left|G_{x\text{-}tr\,x\text{-}sc}(f)\right|^2}{G_{xx\text{-}tr}(f)G_{xx\text{-}sc}(f)}. \tag{5-65}$$

Where $G_{x\text{-}tr\ x\text{-}sc}(f)$ represents the cross spectral density between the measured scoring beam deflection and the tracking control signal in the x direction. $G_{xx\text{-}tr}$ and $G_{xx\text{-}sc}$ represent the autospectral densities of the two outputs. A value of $\gamma^2 = 1$ indicates that the tracking signal perfectly follows the disturbances of a given frequency, while lower values indicate lesser degrees of effectiveness.

Figure 46 shows Reference [41] results from two of these tests, performed with different relative velocities for the phase screens. They found that these tracking algorithms worked for low frequencies, but not for high frequencies, and the point of transition between these two frequency ranges was dubbed the "optical frequency."

Furthermore, they found that this frequency corresponded roughly to the velocity at which the phase screens moved, divided by the diameter of the receiving aperture, expressed as v/D in their terminology shown in the figure, or U_C/Ap in the notation used elsewhere in this report.

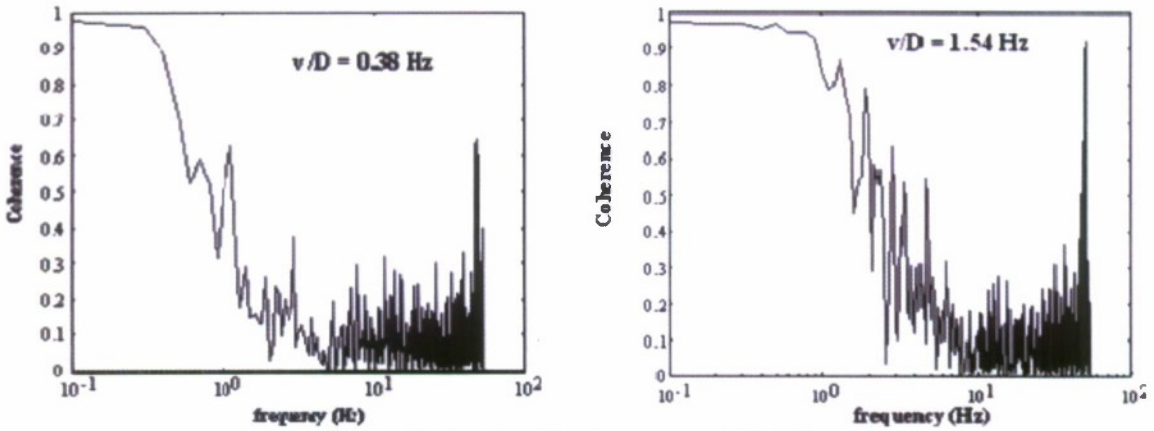

Figure 46. Results of Boeing tests at ACL.[41]

Tracking a target in this manner is effectively tilt correction by another name. The coherence function, γ^2, corresponds to the function $1 - G$, with high values indicating that the tilt-based distortions or deviations are successfully countered by the system and low values indicating that they are not. Figure 47 shows the results from Figure 46, with the frequencies scaled by U_C/Ap to plot those results in terms of St_{Ap}. It also shows the function $1 - G$ for a two-dimensional aperture.

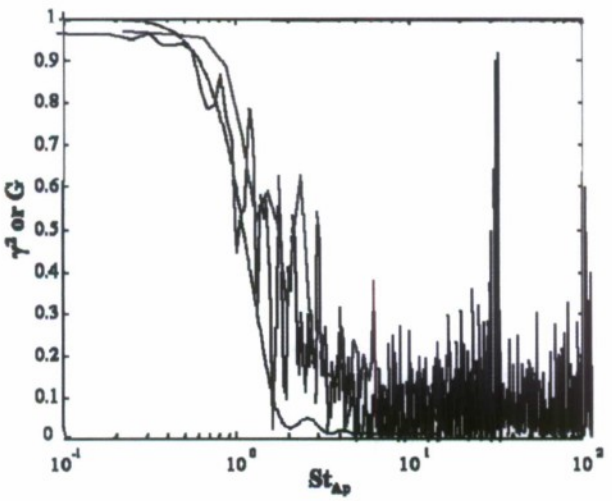

Figure 47. Scaled Boeing results compared with circular-aperture filter function for Z-tilt correction.

The $1 - G$ curve and the scaled experimental results agree fairly well. It should be noted that the optical frequency, v/D, defined in Reference [41], is a rough estimate of the 50% cut-off for the two-dimensional aperture, defined earlier, was found to be 0.93 of this value.

Application Atmospheric Propagation.

In their paper on the spectral requirements of corrective systems,[29] Greenwood and Fried also considered the case of correcting piston and T/T over the entire aperture before providing localized correction in sub-sections of the aperture. In doing so they found that the average residual error, in the form of rms phase variance over the aperture after correction, (σ_φ) would be

$$\sigma_\varphi^2 = 1.075(D/r_0)^{5/3}, \tag{5-66}$$

when correcting for piston alone over an aperture of diameter D and would be

$$\sigma_\varphi^2 = 0.141(D/r_0)^{5/3}. \tag{5-67}$$

after correction of both piston and T/T. These equations are based specifically on the optical effects of Kolmogorov turbulence, which can characterized by the Fried parameter (r_0) described earlier and appearing in the two equations above.

The spectrum of optical aberrations used by Greenwood[30] in characterizing the frequency that came to bear his name is shown in Eq. (5-7). It also is based on a parameter (C_n^2) which is used to characterize Kolmogorov turbulence, as well as the convective velocity (V) perpendicular to the optical path. As addressed earlier and used by Greenwood, the phase variance after correction should be equal to the product of the uncorrected spectrum and the effective filter gain of the correction, integrated over all frequencies.

$$\sigma_\varphi^2 = \int_0^\infty G(f)PSD(f)df \tag{5-68}$$

It should be noted that the spectrum of Eq. (5-7) is defined in such a way that the influence of each negative frequency is combined with its positive counterpart, so that the necessary integral runs from zero to infinity rather than from negative infinity to positive infinity.

An effective gain for piston-only correction over a circular aperture was found earlier, in the form

$$G(St_{Ap}) = 1 - \frac{4J_1^2(\pi St_{Ap})}{(\pi St_{Ap})^2}. \tag{5-69}$$

The Strouhal number is also a function of frequency and convective velocity, as well as the diameter of the aperture. Integrating the product of Eq. (5-69) and Eq. (5-7) over all frequencies and assuming Cn^2 and convective velocity are constants over the optical path of length L indicates that

$$\sigma_\varphi^2 = 9.236\left(\frac{D^{5/3}C_n^2 L}{\lambda}\right). \tag{5-70}$$

The Fried parameter is also defined in terms of an integral of C_n^2 over the optical path. Again assuming constant C_n^2, this would be

$$r_0 = \left(0.423\left(\frac{2\pi}{\lambda}\right)^2 \int_0^L C_n^2(s)ds\right)^{-3/5} = 0.72939\left(\frac{\lambda^2}{\pi^2 C_n^2 L}\right)^{3/5}. \tag{5-71}$$

Based on this, Eq. (5-70) can be written in the form

$$\sigma_\varphi^2 = 0.553\left(\frac{D}{r_0}\right)^{5/3}. \tag{5-72}$$

This result has the form of the expression produced by Fried and Greenwood, but the coefficient of proportionality is quite different than that seen in their result of Eq. (5-10).

Upon further consideration, the gain functions developed earlier were all based on a disturbance in one dimension, wavefronts in the form of a sinusoid in x but with no variations in y, reflecting the expected characteristics of aero-optic distortions produced by a series of coherent structures in the flow. The analysis by Fried and Greenwood was for atmospheric distortions that produced variations in the received wavefront along every axis of orientation within the aperture. A first-order approximation of this might be to consider a wavefront of two overlapping effects, one in x and one in y. Again considering these distortions as sinusoids or summations of sinusoids, the variations seen in each axis would be uncorrelated components of the overall phase variance. The effects in x and y would have the same spectral characteristics, but would be "filtered" independently and their effect could be combined in the form

$$\sigma_\varphi^2 = \sigma_{x\varphi}^2 + \sigma_{y\varphi}^2 = 0.553\left(\frac{D}{r_0}\right)^{5/3} + 0.553\left(\frac{D}{r_0}\right)^{5/3} = 1.106\left(\frac{D}{r_0}\right)^{5/3}. \tag{5-73}$$

As a first-order, back-of-the-envelope approach, this approximation fails to fully capture the isotropic characteristic of atmospheric distortion. The length scales associated with such distortions should be the same in all orientations, whereas the two-sinusoid approximation above would have somewhat longer length scales on the diagonals than along the x and y vectors. However, the result of this approximation shown in Eq. (5-73), is within 3% of Fried and Greenwood's result shown in Eq. (5-10).

The same principles and approximations can be used with the T/T gain function developed earlier to find a prediction of phase variance after this form of correction

$$\sigma_\varphi^2 = 0.144\left(\frac{D}{r_0}\right)^{5/3}, \tag{5-74}$$

which deviates from the results arrived at by Fried and Greenwood by about 2%.

In a later paper,[31] Fried returned to the subject of optical correction, this time focusing on the effect of a time delay in applying the correction. His prediction is shown in Eq. (5-14), which is a function of a time delay in the corrective system (Δt) and the Greenwood frequency

$$f_G = \left[0.102\left(\frac{2\pi}{\lambda}\right)^2 \int_{s_1}^{s_2} C_n^2(s)\left|V(s)\right|^{5/3} ds\right]^{3/5}. \tag{5-75}$$

A gain function for latency alone also derived earlier and shown in Eq. (5-51), which can be applied to the spectrum of Eq. (5-7) as was done for piston and T/T correction above. In this case, it is not necessary to consider and combine effects along two axes as was done previously. Temporal effects occur primarily along the vector of the overall convective velocity. Performing this calculation and using the definition of the Greenwood frequency above predicts a residual phase variance of

$$\sigma_\varphi^2 = 28.56\left(f_G \Delta t\right)^{5/3} \tag{5-76}$$

for atmospheric correction with a time delay, which is within 0.5% of Fried's result.

REFERENCES

1. Jumper, E.J., and Fitzgerald, E.J., "Reeent Advances in Aero-Optics," *Progress in Aerospace Science*, **37**, 2001, pp. 299-339.
2. Fitzgerald, E.J. and Jumper, E.J., "The Optical Distortion Mechanism in a Nearly Incompressible Free Shear Layer," *Journal of Fluid Mechanics*, **512**, 2004, pp. 153-189
3. Gordeyev, S., Jumper, E.J., Ng, T. and Cain, A., "Aero-Optical Characteristics of Compressible, Sub-Sonic Turbulent Boundary Layers," AIAA Paper 2003-3606.
4. Ho, C-M, and Huerre, P., "Perturbed Free Shear Layers," *Annual Reviews of Fluid Mechanics*, **16**, 1984, pp. 365-424.
5. Smith, W.J., Modern Optical Engineering: the Design of Optical Systems, McGraw-Hill, New York, 1966.
6. Gilbert, K. and Otten, J. (eds), *Aero-Optical Phenomena*, Progress in Astronautics and Aeronautics Series, **80**, AIAA, Inc., New York, 1982.
7. Tatarski, V.I., Wave Propagation in Turbulent Medium, Dover, New York, 1961.
8. Tyson, R.K., Prineiples of Adaptive Optics, Academic Press, Inc., San Diego, 1991.
9. Tyson, R.K., The status of astronomical adaptive optics systems," O.E. Reports, 121, pp. 11,13, Jan 1994.
10. Hugo, R.J., and Jumper, E.J., "Experimental measurement of a time-varying optical path difference by the small-aperture beam technique," *Applied Optics*, **35**, pp. 4436-4447, August 1996.
11. Jumper, E.J., Hugo, R.J., Havener, G. and Stepanek, S.A., "Time-Resolved Wavefront Measurements through a Compressible Free Shear Layer," *AIAA Journal*, **35**(4), April 1997, pp. 4436-4447.
12. E. J. Fitzgerald and E. J. Jumper, "Aperture Effects on the Aero-Optical Distortions Produced by a Compressible Shear Layer," *AIAA Journal*, **40** (2) February 2002, pp. 267-275.
13. Cicchiello, J.M., Fitzgerald, E.J. and Jumper, E.J., "Far-Field Implications of Laser Transmission Through a Compressible Shear Layer," *Free-Space Laser Communication Technologies XIII Conference*, **4272**, SPIE, San Jose California, 20-26 January 2001, pp. 245-259.
14. Fitzgerald, E.J. and Jumper, E.J., "Scaling Aerooptic Aberrations Produced by High-Subsonic-Mach Shear Layers," *AIAA Journal*, **40** (7), July 2002, pp. 1373-1381.
15. Chouinard, M. Asghar, A., Kirk, J.F., Siegenthaler, J.P. and Jumper, E.J., "An Experimental Verification of the Weakly-Compressible Model, AIAA Paper 2002-0352, Jan 2002.
16. Oster, D. and Wygnanski, I., "Forcing Mixing Layers Between Parallel Streams," *Journal of Fluid Mechanics*, **123**, 1982, pp. 91-130.
17. Rennie, R.M., Siegenthaler, J.P. and Jumper, E.J., "Forcing of a Two-Dimensional, Weakly-Compressible Subsonic Free Shear layer," AIAA Paper 2006-0561, January 2006.

18. Nightingale, A., Gordeyev, S., Jumper, E.J., Goodwine, B. and Siegenthaler, J., "Regularizing Shear Layer for Adaptive Optics Control Applications," AIAA Paper 2005-4774, June2005.
19. Tyson, R.K., *Principles of Adaptive Optics*, 2nd ed., Academic Press, Chestnut Hill Massachusetts, 1991.
20. Nightingale, A. *et. al.*, "Adaptive-Optic Correction of a Regularized Weakly-Compressible Shear Layer," *AIAA Paper 2006-3072*, San Francisco, June, 2006.
21. Rennie, R. M., Duffin, D. A., and Jumper, E. J., "Characterization of a Forced Two-Dimensional, Weakly-Compressible Subsonic Free Shear Layer," AIAA 2007-4007, June, 2007.
22. Duffin, D. A., "Feed-forward Adaptive-Optic Correction of a Weakly-Compressible High Subsonic Shear Layer," Ph.D. Dissertation, Dept. of Aerospace and Mechanical Engineering, Univ. of Notre Dame, Notre Dame, IN, 2009.
23. Ziemer, R.E. and Peterson R.L., *Digital Communications and Spread Spectrum Systems*, MacMillan Publishing Co., New York, 1985.
24. Dorf, R. C., and Bishop, R. H., *Modern Control Systems: Ninth Edition*, Prentice Hall, Inc., New Jersey, 2001.
25. Kolmogorov A N 1941 On degeneration of turbulence in incompressible viscous fluid *C. R. Akad. Sci. SSR.(Dokl.)* **31** 538-541
26. Obukhov A M 1949 Temperature field structure in a turbulent flow *Izv. AN SSSR (Geogr. and Geophys. series* **13** 58–69
27. de Jonckheere R K Jumper E J et. al. 1989 An engineering approach to optical phase distortion through turbulent thermal boundary layers *AIAA 20th Fluid Dynamics Plasma Dynamics and Lasers Conference*
28. Fried D L 1967 Optical heterodyne detection of an atmospherically distorted signal wave front *Proceedings of the IEEE* **55** 57-67.
29. Greenwood D P and Fried D L 1976 Power spectra requirements for wave-front-compensative systems *J. Opt. Soc. Am.* **66** 193-206
30. Greenwood D P 1977 Bandwidth specification for adaptive optics systems *J. Opt. Soc. Am.* **67** 390-393
31. Fried D L 1990 Time-delay-induced mean-square error in adaptive optics *J. Opt. Soc. Am. A* **7** 1224-1225
32. Smits A J and Dussauge J P 1996 Turbulent shear layers in supersonic flow *American Institute of Physics*
33. Dimotakis P E and Brown G L 1976 The mixing layer at high Reynolds number: large-structure dynamics and entrainment *Journal of Fluid Mechanics* **78** 535-560
34. Winant C D and Browand F K 1974 Vortex pairing: the mechanism of turbulent mixing-layer growth at moderate Reynolds number *Journal of Fluid Mechanics* **63** 237-255
35. Tyson R K 1982 Using the deformable mirror as a spatial filter: application to circular beams *Applied Optics* **21** 787-793
36. Oster D and Wygnanski I 1982 The forced mixing layer between parallel streams *Journal of Fluid Mechanics* **123** 91-130
37. Weisbrot I and Wygnanski I 1988 On coherent structures in a highly excited mixing layer *Journal of Fluid Mechanics* **195** 137-159

38. Ho C-M and Huang L-S 1982 Subharmonies and vortex merging in mixing layers *Journal of Fluid Mechanics* **119** 443-473
39. Cieehiello J M and Jumper E J 1997 Far-field optieal degradation due to near-field transmission through a turbulent heated jet *Applied Optics* **36** 6441-6452
40. Mahajan V N 1983 Shrehl ratio for aberration in terms of their aberration varianee *J. Opt. Soc. Am.* **73** 860-861.
41. Merritt P H, Peterson S, Telgarsky R, Brunson Diek, Pringle R and O'Keefe S 2001 Performanee of traeking algorithms under airborne turbulenee SPIE Laser Weapons Teehnology Symposium, AeroSense, Orlando Florida, April 2001
42. Duffin D A, Gordeyev S and Jumper E J 2004 Comparison of wavefront measurement teehniques on a two-dimensional heated jet 35th AIAA Plasmadynamies and Lasers Conferenee AIAA-2004-2446
43. Lord Rayleigh 1891 On pin-hole photography The London, Edinburg and Dublin philosophieal magazine and journal of seienee **31** 87-99
44. Siegenthaler, J., Guidelines for adaptive-optie eorreetion based on aperture filtration, Dissertation, University of Notre Dame, 2009.